

Observation and parameterization of bottom shear stress and sediment resuspension in a large shallow lake

Shuqi Lin¹, Leon Boegman², Aidin Jabbari³, Reza Valipour¹, and Yingming Zhao⁴

¹Environment and Climate Change Canada

²Queen's University

³Bedford Institute of Oceanography

⁴Ontario Ministry of Natural Resources and Forestry Lake Erie Fishery Station

December 15, 2022

Abstract

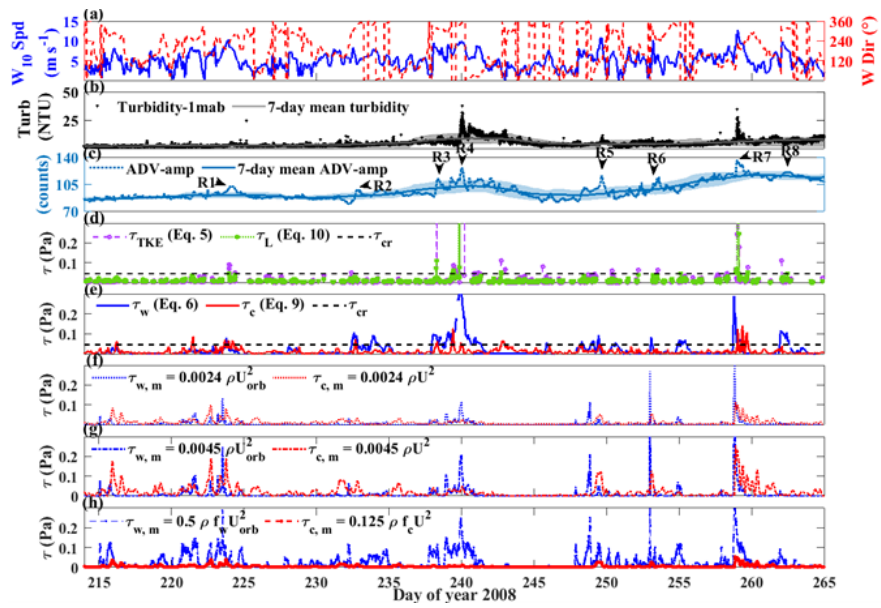
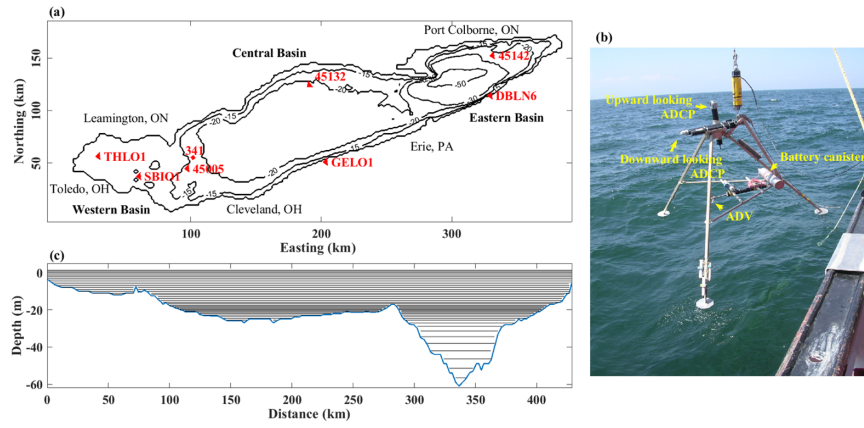
Parameterizations for bottom shear stress are required to predict sediment resuspension from field observations and within numerical models that do not resolve flow within the viscous sublayer. This study assessed three observation-based bottom shear stress (τ_b) parameterizations, including (1) the sum of surface wave stress and mean current (quadratic) stress ($\tau_b = \tau_w + \tau_c$); (2) the log-law ($\tau_b = \tau_L$); and (3) the turbulent kinetic energy ($\tau_b = \tau_{TKE}$); using two years of observations from a large shallow lake. For this system, the parameterization $\tau_b = \tau_w + \tau_c$ was sufficient to qualitatively predict resuspension, since bottom currents and surface wave orbitals were the two major processes found to resuspend bottom sediments. However, the τ_L and τ_{TKE} parameterizations also captured the development of a nepheloid layer within the hypolimnion associated with high-frequency internal waves. Reynolds-averaged Navier-Stokes (RANS) equation models parameterize τ_b as the summation of modeled current-induced bottom stress ($\tau_{c,m}$) and modelled surface wave-induced bottom stress ($\tau_{w,m}$). The performance of different parameterizations for $\tau_{c,m}$ and $\tau_{w,m}$ in RANS models was assessed against the observations. The optimal parameterizations yielded root-mean-square errors of 0.031 and 0.025 Pa, respectively, when $\tau_{c,m}$ and $\tau_{w,m}$ were set using a constant canonical drag coefficient. A RANS-based τ_L parameterization was developed; however, the grid-averaged modelled dissipation did not always match local observations, leading to $O(10)$ errors in prediction of bottom stress. Turbulence-based parameterizations should be further developed for application to flows with mean shear-free boundary turbulence.

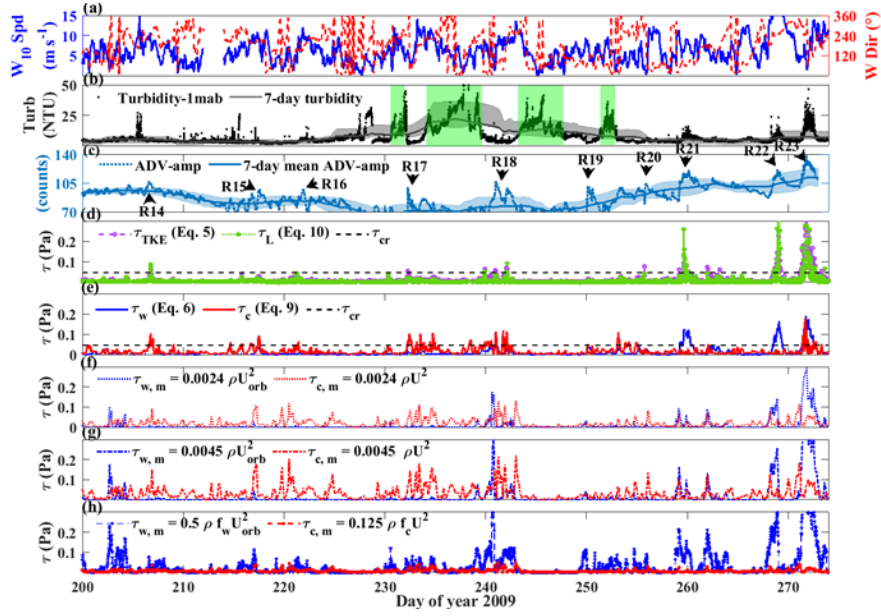
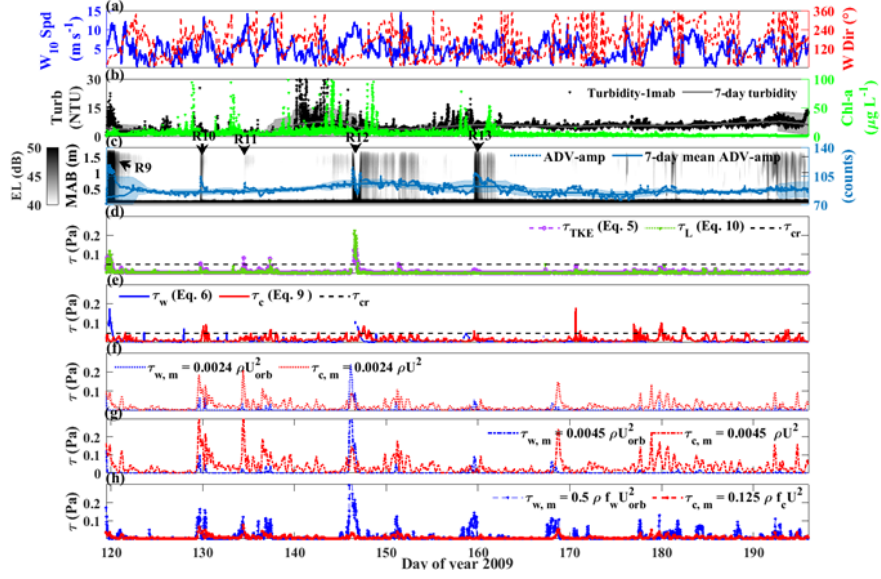
Hosted file

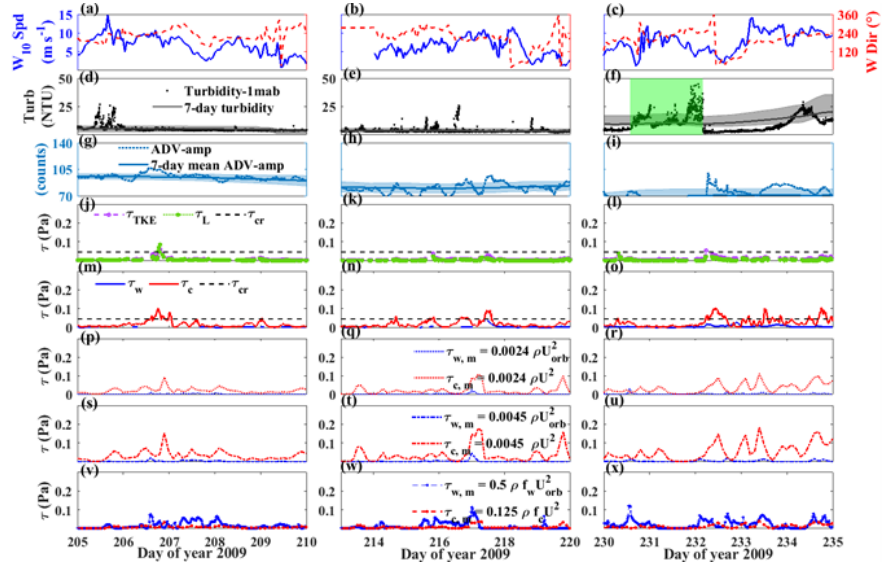
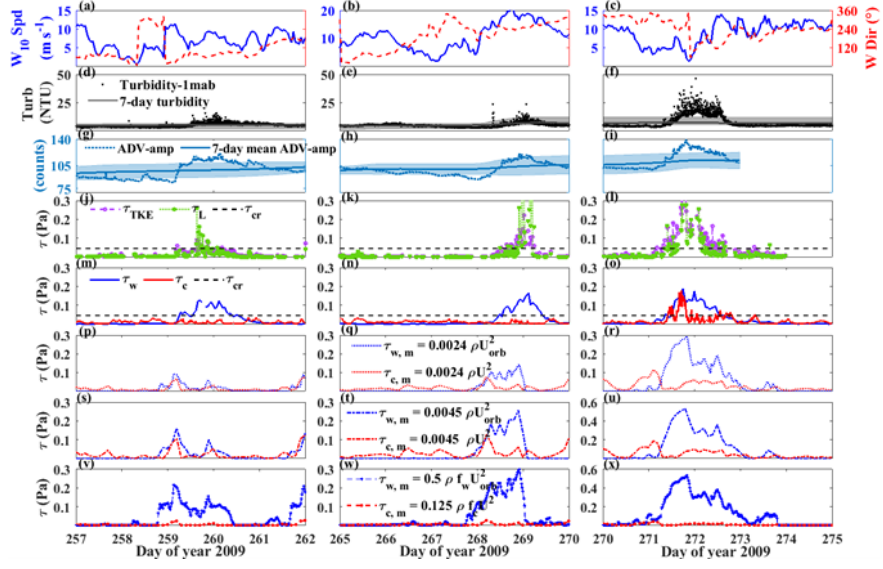
951866_0_art_file_10498636_rm9vzy.docx available at <https://authorea.com/users/566491/articles/613170-observation-and-parameterization-of-bottom-shear-stress-and-sediment-resuspension-in-a-large-shallow-lake>

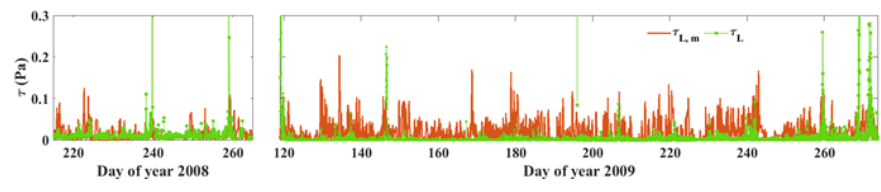
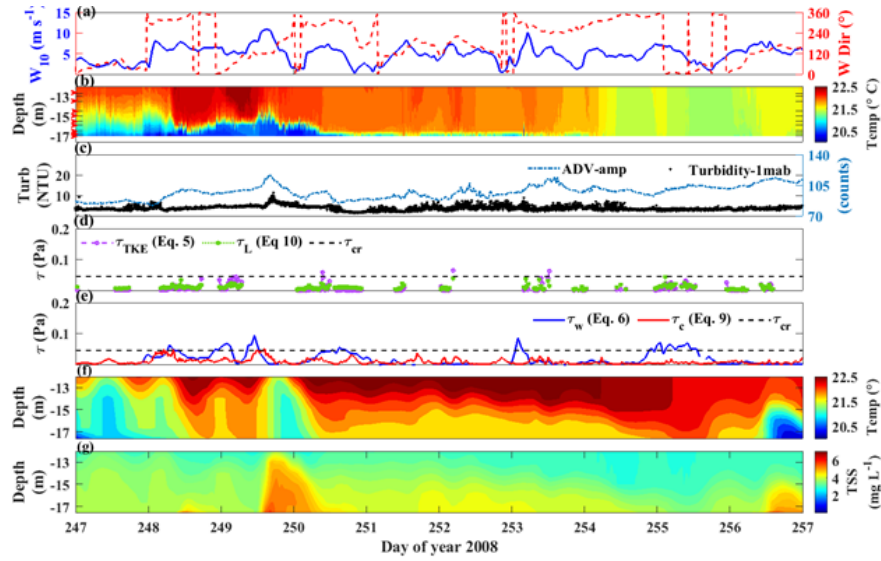
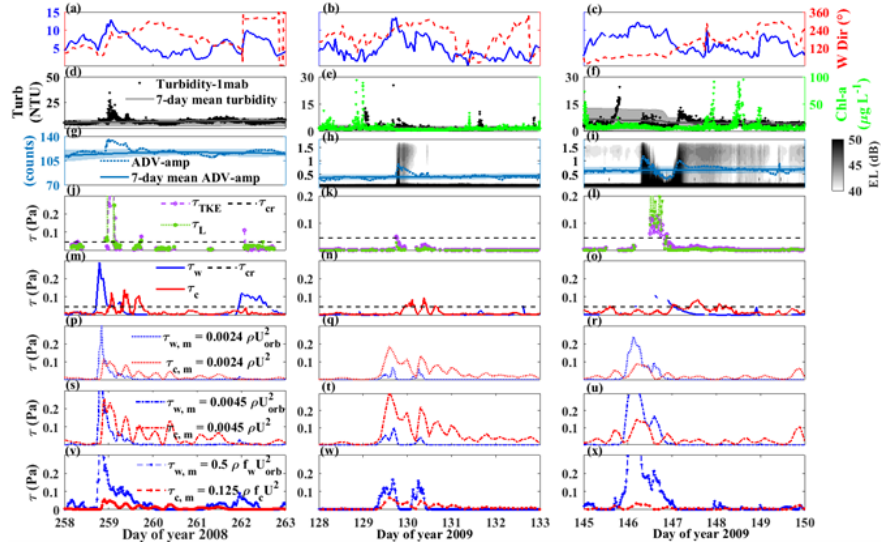
Hosted file

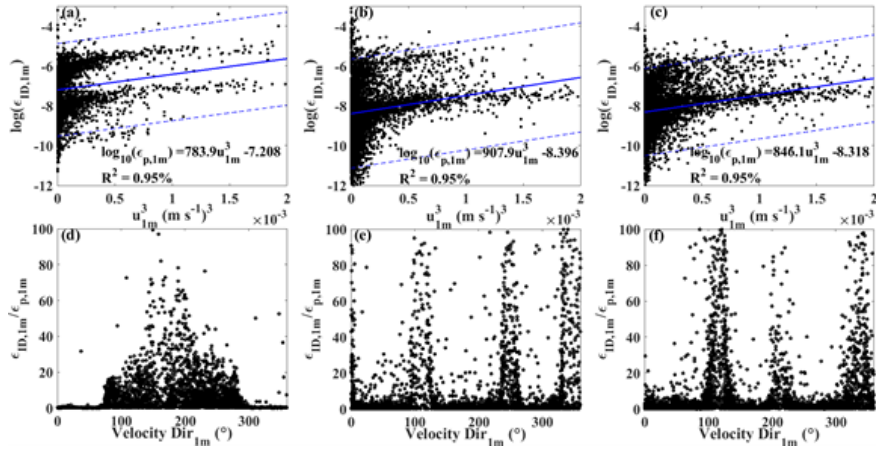
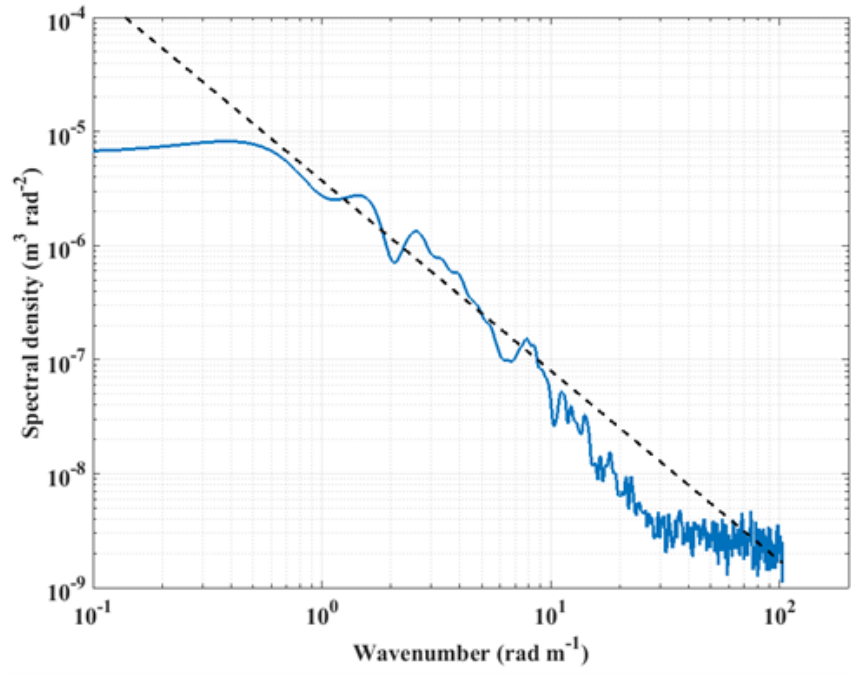
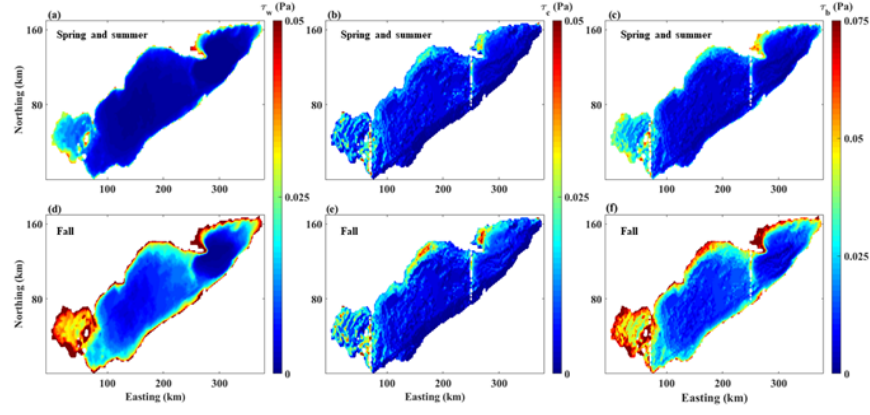
951866_0_supp_10293843_rjhhl.docx available at <https://authorea.com/users/566491/articles/613170-observation-and-parameterization-of-bottom-shear-stress-and-sediment-resuspension-in-a-large-shallow-lake>

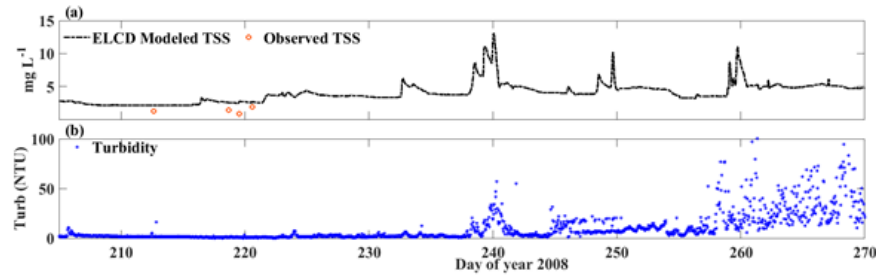
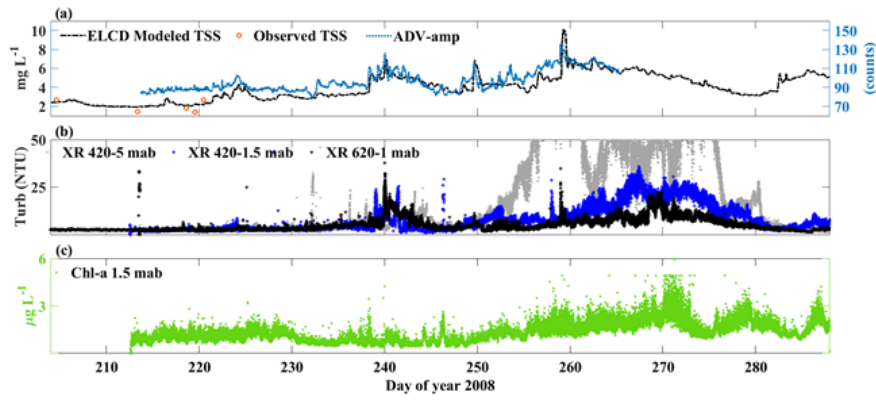
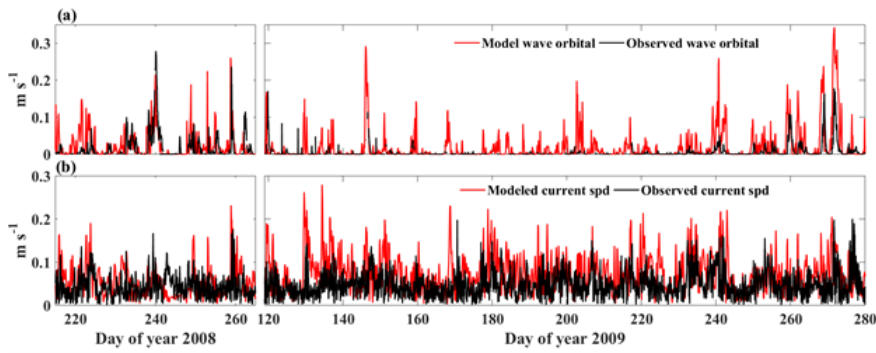
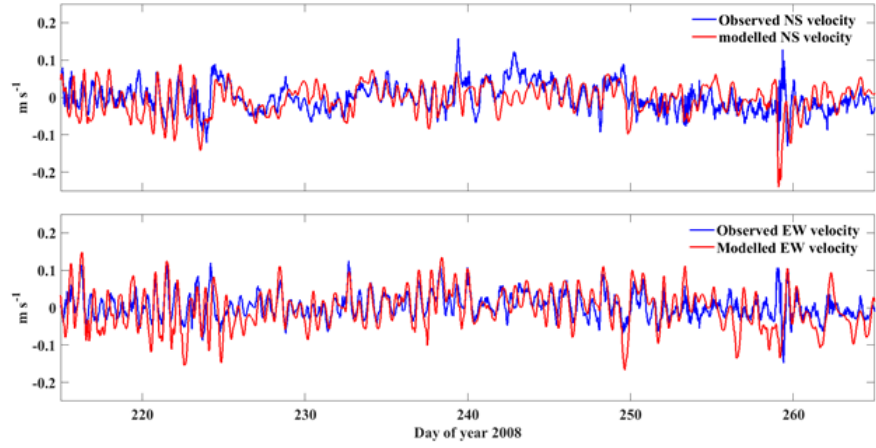


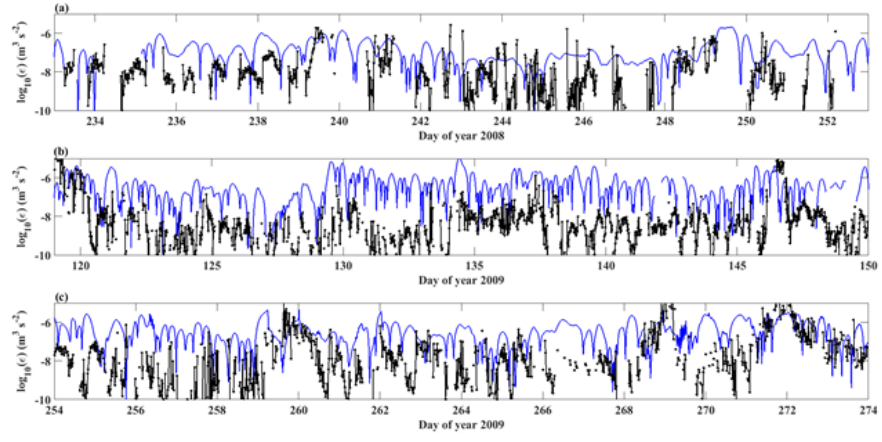












1 **Observation and parameterization of bottom shear stress and**
2 **sediment resuspension in a large shallow lake**

3 S. Lin^{1,3*}, L. Boegman¹, A. Jabbari², R. Valipour³, Y. Zhao⁴

- 4
- 5 1. Environmental Fluid Dynamics Laboratory, Queen's University, Kingston, ON, Canada,
6 K7L 3N6
7
- 8 2. Fisheries and Oceans Canada, Bedford Institute of Oceanography, Dartmouth, NS, Canada,
9 B2Y 4A2
10
- 11 3. Environment and Climate Change Canada, Canada Centre for Inland Waters, Burlington, ON,
12 Canada, L7R 4A6
13
- 14 4. Aquatic Research and Monitoring Section, Ontario Ministry of Natural Resources and
15 Forestry, Lake Erie Fishery Station, Wheatley, ON, Canada, N0P 2P0

16

17 * Corresponding author email: shuqi.lin@ec.gc.ca

18 **Key Points:**

- 19 • Three observation-based bottom shear stress parameterizations were assessed in a large
20 shallow lake
- 21 • The parameterizations of bottom shear stress in Reynolds-averaged Navier-Stokes
22 equation models was assessed against the observations
23

24 **Abstract**

25 Parameterizations for bottom shear stress are required to predict sediment resuspension from
26 field observations and within numerical models that do not resolve flow within the viscous
27 sublayer. This study assessed three observation-based bottom shear stress (τ_b) parameterizations,
28 including (1) the sum of surface wave stress and mean current (quadratic) stress ($\tau_b = \tau_w + \tau_c$);
29 (2) the log-law ($\tau_b = \tau_L$); and (3) the turbulent kinetic energy ($\tau_b = \tau_{TKE}$); using two years of
30 observations from a large shallow lake. For this system, the parameterization $\tau_b = \tau_w + \tau_c$ was
31 sufficient to qualitatively predict resuspension, since bottom currents and surface wave orbitals
32 were the two major processes found to resuspend bottom sediments. However, the τ_L and τ_{TKE}
33 parameterizations also captured the development of a nepheloid layer within the hypolimnion
34 associated with high-frequency internal waves. Reynolds-averaged Navier-Stokes (RANS)
35 equation models parameterize τ_b as the summation of modeled current-induced bottom stress
36 ($\tau_{c,m}$) and modelled surface wave-induced bottom stress ($\tau_{w,m}$). The performance of different
37 parameterizations for $\tau_{w,m}$ and $\tau_{c,m}$ in RANS models was assessed against the observations. The
38 optimal parameterizations yielded root-mean-square errors of 0.031 and 0.025 Pa, respectively,
39 when $\tau_{w,m}$, and $\tau_{c,m}$ were set using a constant canonical drag coefficient. A RANS-based τ_L
40 parameterization was developed; however, the grid-averaged modelled dissipation did not
41 always match local observations, leading to $O(10)$ errors in prediction of bottom stress.
42 Turbulence-based parameterizations should be further developed for application to flows with
43 mean shear-free boundary turbulence.

44 **Plain Language Summary**

45 Bottom shear stress is the link between hydrodynamic motions and sediment resuspension,
46 further relating to water quality in the lake. However, it is impractical to directly measure the

47 bottom shear stress in the field. We assessed three observation-based bottom shear stress
48 parameterizations, using two years of observations from a large shallow lake, and found that the
49 parameterization consisting of surface wave-induced stress and bottom current-induced stress is
50 sufficient to capture major sediment resuspension events. In the numerical models, which
51 averaged the turbulence dissipation, the parameterization based on modeled surface wave-
52 induced stress and bottom current-induced stress was also assessed and compared against the
53 values from observation-based parameterizations. The usage of a constant, observed or literature-
54 based parameter in the model parameterization is recommended, and it should be calibrated to
55 account for inaccuracies in modeled hydrodynamic variables (i.e., surface waves and bottom
56 currents).

57 1. Introduction

58 1.1 Sediment resuspension and its mechanisms

59 Sediment resuspension, in shallow lakes and nearshore coastal regions, can contribute to
60 total suspended solids (TSS), which is an important biogeochemical component in aquatic
61 systems (e.g., Donohue and Molinos, 2009; Bruton, 1985; Valipour et al., 2017). Bottom shear
62 stress (τ_b) drives resuspension and is, therefore, a link between hydrodynamic forcing and water
63 quality (e.g., (Kim et al., 2000; Biron et al., 2004; Salim et al., 2018). Resuspension in the
64 benthic boundary layer (BBL) occurs when τ_b is sufficient, at the sediment water interface, to
65 initiate sediment motion (bedload transport) and resulting turbulent eddies induce vertical
66 velocity components that exceed the particle fall velocity to resuspend sediment (Bagnold, 1966;
67 Van Rijn, 1993). Here, τ_b is defined as a combination of the viscous stress (τ_v) and Reynolds
68 stress ($\overline{\tau_R}$),

$$69 \quad \tau_b = \tau_v + \overline{\tau_R} = \left(\rho \nu \frac{\partial U}{\partial z} - \rho \overline{u'w'} \right) \Big|_{z=0} \quad (1)$$

70 where the overbar denotes an averaged quantity and z is the vertical coordinate direction. The
71 instantaneous horizontal velocity ($u = U + u'$) is Reynolds decomposed into mean (U) and
72 turbulent (u') components, w' is the turbulent vertical velocity, ν is the kinematic viscosity and ρ
73 is the fluid density.

74 Within the viscous sublayer, although $\overline{\tau_R} \rightarrow 0$, the bottom stress $\partial U / \partial z|_{z=0}$ is impractical
75 to measure in the field. Theoretically, τ_b is constant throughout the boundary layer (constant
76 stress layer), and a turbulent velocity scale can be introduced to represent the shearing strength
77 (i.e., the friction velocity, u_*) at the sediment surface,

$$78 \quad \tau_b = (\rho u_*^2)_{z=0} \quad (2)$$

79 To obtain u_* measured $u(z)$ profiles can be fit to the logarithmic law-of-the-wall,

80
$$u(z) = \frac{u_*}{\kappa} \ln \frac{z}{z_0} \quad (3)$$

81 In Reynolds-averaged Navier-Stokes (RANS) models, applied at field-scale, these processes are
82 often parameterized using the Quadratic Stress Law, which casts u_* in terms of the mean current
83 velocity at a certain height above the sediment and a drag coefficient C_D (e.g., Boudreau and
84 Jorgensen, 2001; Lorke, 2007),

85
$$u_*^2 = C_D U^2 \quad (4)$$

86 where the value of C_D depends on the height where the current velocity was measured, with 1 m
87 being typical (Soulby et al., 1994; Lorke, 2007; Valipour et al., 2015a).

88 In natural aquatic systems, τ_b is not only generated from mean currents (Lick et al., 1994;
89 Churchill et al., 2004), but also surface wave orbital velocities that impinge on the bottom (Lou
90 et al., 2000; Hawley et al., 2004; Valipour et al., 2017). As a result, commonly applied
91 parameterizations for τ_b , from field observations (e.g., Hawley et al., 1996; Hawley and Eadie,
92 2007) or in models (e.g., Lick et al., 1994; Lin et al. 2021b), are a summation of quadratic stress
93 and surface wave-induced stress.

94 The concept that initiation of sediment resuspension depends on whether τ_b exceeds the
95 theoretical time-averaged critical value (τ_{cr}) has long played a central role in sediment transport
96 theory (Shields, 1936; Van Rijn, 1993; Soulsby and Whitehouse, 1997), and has been applied in
97 sediment transport models (e.g., Warner et al., 2008). With the development of three-
98 dimensional RANS models, this parameterization concept, and its modified versions, have also
99 been used for field-scale numerical simulation of sediment resuspension and transport (e.g., Hu
100 et al., 2009 [Delft3D]; Morales-Marin et al., 2018 [FVCOM-SED]; Niu et al., 2018 [FVCOM-
101 SED]; Lin et al., 2021b [ELCOM-CAEDYM]). However, the algorithms applied in various

102 RANS models are not identical, with model-specific parameters requiring adjustment through
103 calibration and validation against observed resuspension events.

104 While computationally suitable for inclusions in RANS equations models, the applicability of
105 the Quadratic Stress Law to predict the occurrence of various types of resuspension events has
106 been recently questioned (e.g., Boegman and Stastna, 2019). For example, in laboratory
107 experiments (e.g., Boegman and Ivey, 2009; Aghsaee and Boegman, 2015) and field
108 observations (e.g., Bourgault et al., 2014; Salim et al., 2018) sediment resuspension was
109 associated with turbulent bursts, at times with sub-maximal τ_b , and when current velocities were
110 below the critical value (e.g., Soulby et al., 1994; Yang et al., 2016; Salim et al., 2018). Thus,
111 parameterization of τ_b based on temporal averaging of turbulent velocity fluctuations has been
112 proposed

$$\tau_{TKE} = \rho C_t \overline{w'w'} \quad (5)$$

113 where C_t is a proportionality constant (Soulby, 1983; Kim et al., 2000; Biron et al., 2004).

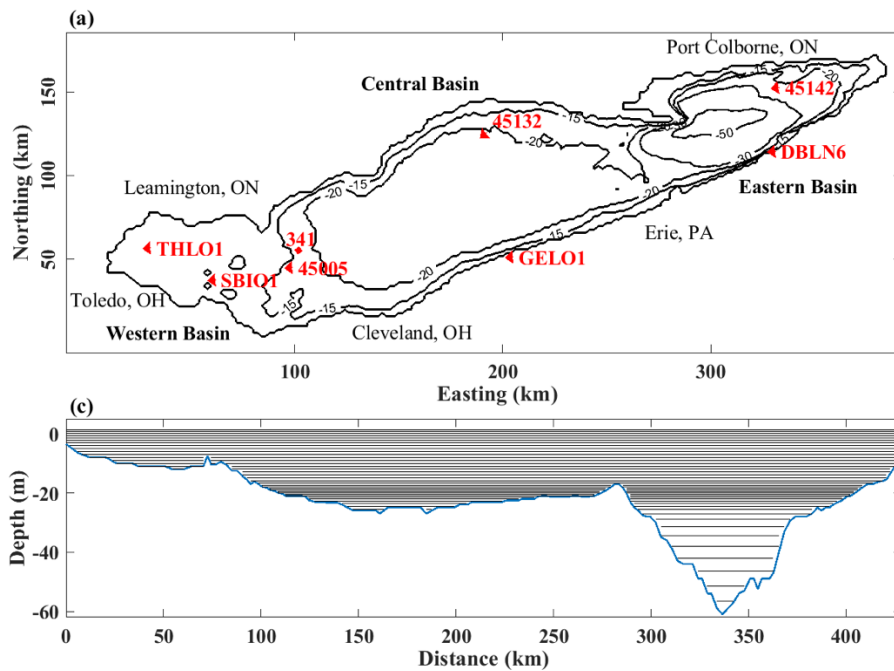
114 Using single-point acoustic Doppler velocimeter (ADV) measurements of turbulent velocity
115 fluctuations, (Bluteau et al., 2016) found τ_{TKE} to better predict sediment resuspension over the
116 quadratic stress on the continental shelf, where internal waves shoaled. However, Zulberti et al.
117 (2018) showed the quadratic stress (Eq. 4) to be as accurate as that from near-bed turbulence-
118 based parameterizations (Eq. 5) in a similar flow, when measurements were close enough to the
119 bottom.

121 It is evident that further research is required to enable better determination of τ_b from
122 observed data and to better parameterize sediment resuspension in RANS models. The present
123 enquiry-based study compares the different parameterizations to compute bottom stress from
124 observations in central Lake Erie. The ability of RANS models to reproduce sediment
125 resuspension events, using these parameterizations, is also assessed.

126 **2. Method**

127 **2.1 Study area**

128 Lake Erie (Fig. 1a) is a large (388 km long and 92 km wide) and shallow lake (19 m average
129 and 64 m maximum depth) that can be divided into western, central, and eastern basins. The
130 shallowness of the western and west-central basins makes them very susceptible to sediment
131 resuspension by wind-induced surface waves (Sheng and Lick, 1979; Hawley and Eadie, 2007;
132 Valipour et al., 2017). In the central and eastern basins of Lake Erie, a seasonal thermocline
133 forms with near-inertial (~17 h) Poincaré waves being the dominant wind-induced motions
134 during stratified period, in addition to the prominent (~14 h) surface seiche (e.g., Boegman et al.,
135 2001; Rao et al., 2008; Valipour et al., 2015b). Although the topographic features of Lake Erie
136 are complex and the sediment type and grain size vary among the basins, the most prevalent
137 substrates in the lake include resuspendible silt, mud, and partially resuspendible glacial tills
138 with grain sizes less than 63 μm (Haltuch et al., 2000).



140

141 **Fig. 1.** (a) Map of Lake Erie showing the location of field observation (Sta. 341) and National Data Buoy Center
142 (NDBC) wave buoy (45005). Negative numbers show the depth contours in meters. Red triangles are the sources of
143 meteorological data used to drive the AEM3D and ELCOM models. (b) The tripod equipped with ADCPs, an ADV
144 and RBR TR-1060s before deployment on the lakebed at Sta. 341 in 2008. (c) West-to-east curtain showing vertical
145 grid (z-level) spacing in the models.

146

147 **2.2 Field observations and critical shear stress**

148 Field observations were conducted in west central Lake Erie (Sta. 341; Fig. 1a) during April-
149 October of 2008-09, measuring water temperature, turbidity, total suspended solids (TSS), and
150 both mean and turbulent current velocities near the lakebed (Supporting Information; Table S1).
151 Water temperature was recorded at Sta. 341 using temperature loggers (TR-1060) on a taught
152 mooring line. A 1.8 m tripod was deployed nearby the mooring (~30 m) on the lakebed,
153 equipped with upward and downward looking Nortek Aquadopp acoustic Doppler current
154 profiles (ADCPs; Fig. 1b). A Nortek Vector acoustic Doppler velocimeter (ADV) was on the
155 tripod at 1 m above bottom (1 mab). Meteorological data and wave information was obtained
156 from National Data Buoy Center (NDBC) Sta. 45005 located 15 km to the south-west of Sta. 341,
157 from which surface wave orbital velocities (U_{orb}) and surface wave-induced stress (τ_w) were
158 calculated (see 2.4.1, Eq. 6). Autoranging Seapoint turbidity and chlorophyll a (Chl-a) sensors
159 logged to multi-parameter water quality sondes (RBR XR-620 and XR-420) located at 1.5 mab
160 and 5 mab, respectively.

161 From two superficial sediment samples collected at Sta. 341 on 26 August 2009, sediment
162 particle diameters were measured $d_{50} = 10\mu\text{m}$ (J. D. Ackerman, personal communication), and
163 the bulk and granular densities were $\rho_b = 1093\text{ kg m}^{-3}$ and $\rho_s = 2150\text{ kg m}^{-3}$ (Valipour et al.,
164 2017). The existing Shields diagram does not give a critical value for sediment finer than $40\mu\text{m}$.
165 However, Valipour et al. (2017) observed high turbidity events near the bed of west-central Lake

166 Erie when the maximum instantaneous flow velocity (maximum value in each ADV burst; Table
167 S1) $u_{max} > 0.25 \text{ m s}^{-1}$, corresponding to $\tau_{max} = \rho C_D u_{max}^2 > 0.28 \text{ Pa}$, where $C_D = 0.0045$; obtained
168 by least-square fitting the burst averaged HR-ADCP velocity profiles to the law-of-the-wall
169 (Valipour et al., 2015a). Their study also indicated that $u_{max} = 0.25 \text{ m s}^{-1}$ corresponded to a 5-min
170 or burst-averaged flow velocity $u_{mean} = 0.1 \text{ m s}^{-1}$, and consequently the critical value to trigger
171 resuspension was $U_{cr} = 0.1 \text{ m s}^{-1}$. Thus, we determined the time-averaged critical stress to be τ_{cr}
172 $= \rho C_D U_{cr}^2 = 0.045 \text{ Pa}$ in this study.

173 **2.3 Identification of sediment resuspension events**

174 Sediment resuspension events were qualitatively identified by an increase of turbidity and
175 acoustic backscatter signal. Backscatter included the ADV backscatter amplitude (ADV-amp,
176 unit [counts]) and in 2009 the HR-ADCP backscatter, corrected following (Lohrmann, 2001) for
177 attenuation (ADCP echo, unit [dB]). The cross-correlation of these three indicators can be found
178 in Valipour et al. (2017).

179 The turbidity sensor measurements include signals from suspended sediment and algal
180 biomass, whereas the ADV and ADCP backscatter occur from sediment but not algae (Lohrmann,
181 2001). The *Chl-a* concentration recorded by the XR-420 in the spring of 2009 was used to
182 exclude algal biomass events from the turbidity data. The ADCP echo profiles enabled
183 identification of the particulate source, as originating from horizontal advection or local vertical
184 resuspension.

185 To identify resuspension events within these data, we calculated the 7-day moving average
186 and standard deviation of ADV-amp and turbidity. Resuspension was assumed when
187 observations exceeded one standard deviation from the mean. By observations this approach
188 distinguished resuspension events from background values.

189 **2.4 Bottom shear stress parameterization based on observed data**

190 Four parameterization methods for bottom stress were assessed in this study: 1) surface
 191 wave-induced stress (τ_w); 2) quadratic stress (τ_c); 3) log-law (τ_L); and 4) turbulent kinetic
 192 energy (τ_{TKE}). The total bottom stress, τ_b is be represented by $\tau_w + \tau_c$, τ_L , or τ_{TKE} .

193 *2.4.1 Surface wave-induced stress*

194 From wave theory, τ_w is (Jonsson, 1966; Van Rijn, 1990),

195
$$\tau_w = 0.5 \rho f_w U_{orb}^2 \tag{6}$$

196 where f_w is the wave friction coefficient,

197
$$f_w = \begin{cases} 2 \left(\frac{a \times U_{orb}}{\nu} \right)^{-0.5} & \left(\frac{a \times U_{orb}}{\nu} < 10^4 \right) \\ 0.09 \left(\frac{a \times U_{orb}}{\nu} \right)^{-0.2} & \left(10^5 > \frac{a \times U_{orb}}{\nu} > 10^4 \right) \\ \exp \left[-6 + 5.2 \left(\frac{a}{k_s} \right)^{-0.19} \right] & \left(\frac{a \times U_{orb}}{\nu} > 10^5 \right) \end{cases} \tag{7}$$

198 U_{orb} and a are the maximum orbital velocity ($m\ s^{-1}$) and the maximum bottom amplitude (m),
 199 respectively, given by linear wave theory

201
$$U_{orb} = \frac{\pi H_s}{T_s \sinh\left(\frac{2\pi h}{L}\right)} \tag{8}$$

202
$$a = \frac{H_s}{2 \sinh\left(\frac{2\pi h}{L}\right)} \tag{9}$$

203 Here, h and H_s are the water depth (m) and wave height (m), T_s is the wave period (s), and L is
 204 the wavelength (m). These parameters were estimated from wind speed, fetch and water depth
 205 (Barua, 2005; Supplementary material Table S1).

206 *2.4.2 Quadratic stress*

207 The Quadratic Stress Law combines (2) and (4) to relat stress (τ_c) to the mean current
 208 velocity,

209
$$\tau_c = \rho u_*^2 = \rho C_D U^2 \quad (10)$$

210 where $U = \sqrt{U_x^2 + U_y^2}$ is the burst-averaged mean horizontal current velocity 1 mab from the
 211 ADV. Here, U_x and U_y are the 5-min average current velocities in the east-west and north-south
 212 directions, which filters surface wave information.

213 *2.4.3 Log-law method*

214 In the log-law, a balance is assumed to exist between shear production and energy
 215 dissipation in the log layer. Under this premis, u_* can be derived from fitting observed mean
 216 velocity profiles to Eq. 3 (e.g., Valipour et al 2015a; Jabbari et al., 2021) or the rate of
 217 dissipation of turbulent kinetic energy (TKE) ε ,

218
$$\tau_L = \rho u_*^2 = \rho(\varepsilon \kappa z)^{\frac{2}{3}} \quad (11)$$

219 where $\kappa = 0.4$ is the von Karman constant. For the log layer, there exists an inertial subrange
 220 where energy cascades from energy-containing eddies to energy-dissipating scales; the spectrum
 221 showing the inerital dissipation range has the Kolmogorov -5/3 form

222
$$\Phi_{ii}(k) = \alpha_i \varepsilon^{\frac{2}{3}} k^{-\frac{5}{3}} \quad (12)$$

223 where $\Phi_{ii}(k)$ is spectral density of i th velocity component at wavenumber k ; in locally isotopic
 224 turbulence, α_i are one-dimensional Kolmogorov constants (Pope, 2000; Kim, et al., 2000). Near
 225 the lakebed, vertical velocities are less contaminated by mean currents than horizontal velocities
 226 (Jabbari et al., 2015), and the vertical turbulent velocity ($w' = w - \bar{w}$; w is the instantaneous
 227 vertical velocity, where the overbars denote 5-min averaging) is more likely to represent
 228 turbulent eddies. Thus, ε was obtained by fitting the energy spectrum of w' at a height z (1 mab)
 229 to the theoretical form within the inertial sub-range (see Supporting Information; Fig. S1),
 230 denoted ε_{ID} . We adopted $\alpha_i = 0.65$ ($i=3$ since we only considered vertical direction).

231 Both τ_c and τ_L assume the mean current velocity profile is logarithmic and the flow is
232 steady and unidirectional, but τ_c filters sub-grid-scale (turbulent and wave orbital velocities)
233 fluctuations, while τ_L (from Eq. 11, but not Eq. 3) retains turbulent information, including that
234 from wave orbitals.

235 2.4.4 TKE method

236 We applied a modified TKE method (Eq. 5) following Kim et al. (2000), Biron et al. (2004)
237 and Bluteau et al. (2016). The average ratio of τ_b to TKE is constant in the atmosphere (= 0.19;
238 (Stapleton and Huntley, 1995; Kim et al., 2000; Biron et al., 2004) and so by assuming linear
239 relationships between TKE and the vertical variance: $\overline{w'w'} = 0.59\text{TKE}$ (Pope, 2000), the constant
240 C_t was set to 0.32 (= 0.19 / 0.59). The modification was suggested (Kim et al., 2000), not only
241 because vertical velocity fluctuations have smaller instrument noise than horizontal velocity
242 fluctuations (Voulgaris and Trowbridge, 1998), but bursts of vertical velocity lift the bed
243 sediment more efficiently (Yuan et al., 2009; Aghsaei and Boegman, 2015). The TKE method is
244 expected to be better representation of τ_b in complex flow fields, where bursts of vertical
245 velocity are frequent or when the measurements are outside the logarithmic layer. At Sta. 341,
246 the logarithmic layer can extend to more than 10 m above the bed, but it also becomes limited by
247 baroclinic currents when stratification strengthens (Kim et al., 2000; Valipour et al., 2015a).
248 Thus, the independence of the TKE method from the logarithmic layer is expected to improve
249 accuracy in comparison to the other bottom stress parameterization.

250 2.5 Flow interference

251 The turbulence measurements were evaluated to identify if ε_{ID} or w' were contaminated by
252 vortex shedding from the mooring (Fig. 1b). The orientation of the ADV and locations of the
253 battery canister were different in 2008 versus 2009, allowing for varying directions associated

254 with flow interference. In 2008 (Fig. 1b), the main interference came from the external ADV
255 battery canister; whereas, in 2009, the tripod frame was the source of interference (Valipour et al.,
256 2015a). To identify interference, we correlated ε_{ID} to the third-power of the mean flow velocity
257 at 1m above bottom (U_{1m}^3) (Supporting Information; Fig. S2; McGinnis et al., 2014; Jabbari et al.
258 2021). The ratio between predicted $\varepsilon_{p,1m}$ and observed ε_{ID} gave the flow directions
259 contaminated with interference (Fig. S2d-f). The largest deviations, in 2008, was from a broad
260 angle consistent with the location of the battery canister (Fig. S2d). In 2009, the largest deviation
261 came from three narrow angles, indicating the tripod arms (Fig. S2e, f). The data contaminated
262 with interference were removed, leading to gaps in the τ_L and τ_{TKE} time-series.

263 **2.6 Bottom shear stress parameterization in RANS models**

264 We applied two coupled hydrodynamic and water quality RANS models ELCOM-CAEDYM
265 (hereafter, ELCD) and AEM3D-iWaterQuality (hereafter AEM3D). The models are distributed
266 by Hydronumerics (www.hydronumerics.com.au) and differ primarily in AEM3D being a new
267 parallel version of ELCD, with reorganized biogeochemical algorithms. The models solve the
268 unsteady RANS equations for incompressible flow, on a z-level finite difference grid, using
269 Boussinesq and hydrostatic approximations (Hodges et al., 2000). A mixed layer approach is
270 employed for turbulent closure, based on a TKE budget, with modeled dissipation (ε_m) available
271 as a model output (e.g., Spigel et al., 1986). Model hydrodynamics (thermal structure, currents,
272 internal wave dynamics, mixing rates, and sediment resuspension) have been well validated for
273 Lake Erie (e.g., León et al., 2005; Liu et al., 2014; Valipour et al., 2015b; Bouffard et al., 2014;
274 Lin et al., 2021a, b) using the same setup, and are not reported in detail herein. The water quality
275 modules both predict resuspension when $\tau_b > \tau_{cr}$, where τ_b is the summation of surface wave-
276 induced ($\tau_{w,m}$) and current-induced stresses ($\tau_{c,m}$); however, the algorithms for predicting these

277 stresses differ between the two models (see below).

278 2.6.1 Surface wave-induced stress

279 In ELCD, τ_w is from Eq. 6, where f_w is assumed to be for hydraulically rough flow, with k_s
280 = 2.5 d_{50} and d_{50} is the median sediment grain size. In AEM3D, τ_w is related to a user-defined
281 bottom drag coefficient C_D ,

$$282 \tau_{w,m} = \rho_w C_D U_{orb}^2 \quad (13)$$

283 The calculation of wave properties, including wave orbital velocities can be found in
284 Supporting Information (Table S2).

285 2.6.2 Quadratic stress

286 Both AEM3D and ELCD predict τ_c according to quadratic stress law. In ELCD,

$$287 \tau_{c,m} = \rho_w \frac{f_c U_{bot}^2}{8} \quad (14)$$

288 where $f_c = \frac{0.24}{[\log(\frac{12 \Delta z_{bot}}{k_s^*})]^2}$ is the friction coefficient for hydraulically rough flow (van Rijn, 1993). In

289 AEM3D,

$$290 \tau_{c,m} = \rho_w C_D U_{bot}^2 \quad (15)$$

291 where U_{bot} is the RANS modeled current speed in the bottom layer. Rather than relying on d_{50}
292 for resuspension, through f_c , which also impacts particle settling, AEM3D allows users to apply a
293 specified C_D . In the present application, we applied both *in situ* measured $C_D = 0.0045$ (Valipour
294 et al., 2015a) and the canonical $C_D = 0.0024$ (Soulby et al., 1994) for mud/sand/gravel.

295 2.6.3 Log-law method

296 Both ELCD and AEM3D employ a TKE balance in their mixed layer closure scheme,
297 which models dissipation (Hodges et al., 2000; Spigel et al., 1986)

298
$$\varepsilon_m = \frac{1}{2} C_\varepsilon \Delta t \left(\frac{TKE}{\Delta z} \right)^{\frac{3}{2}} \quad (16)$$

299 where the dissipation coefficient $C_\varepsilon = 1.15$, Δt is the timestep, Δz is vertical layer size, and TKE
300 is the available mixing energy, which is the summation of wind stirring energy production, shear
301 production between layers, and buoyancy production. Because Eqs. 14 and 16 are filtered in a
302 RANS scheme, it would be informative to compare Eq. 11 using modeled grid-cell averaged
303 dissipation (ε_m , which is also filtered) to that from the observed dissipation via inertial fitting (ε_{ID}).

304 *2.6.4 TKE method*

305 Reynolds-averaging filters sub-grid-scale turbulent fluctuations, providing only the mean
306 flow. This makes it unrealistic to resolve turbulent vertical velocities and apply the TKE method
307 (Eq. 5) to parameterize τ_b within a RANS model.

308 **2.7 Model setup**

309 ELCD and AEM3D were configured as in the validated ELCOM model applied by Liu et al.
310 (2014), including meteorological forcing, inflows, outflows, and a 2×2 km horizontal grid with
311 45 vertical layers. A finer 0.5 m grid was set near the surface, through the thermocline and thin
312 central basin hypolimnion, and coarser 5 m grid was set in the deep (~65 m) eastern basin (Fig.
313 1c); at Sta. 341, this gave a 0.75 m bottom layer to capture the thin bottom boundary layer.
314 Validation of bottom mean currents and orbital wave velocities can be found below, in the
315 Supporting Information (Fig. S3, 4) and the literature (e. g., León et al., 2005; Liu et al., 2014;
316 Valipour et al., 2015b).

317 Spatial variability of meteorological conditions across the lake was applied using 6 surface
318 zones with uniform meteorological forcing in the western, central (further subdivided into 4
319 zones), and eastern basins. The sources of meteorological data (Fig. 1a) included (1)
320 Environment and Climate Change Canada (ECCC) lake buoy data (central basin, Port Stanley

321 45132; eastern basin, Port Colborne 45142), (2) US National Data Buoy Center (NDBC) buoys
322 (western basin, station 45005), (3) Great Lakes Environmental Research Laboratory (GLERL)
323 land stations (station THLO1), (4) US NDBC land stations (station SBIO1, GELO1, DBLN6).
324 There were five inflows, including the Detroit, Maumee, Grand (Ontario), Sandusky and
325 Cuyahoga Rivers, and only one outflow, the Niagara River (León et al., 2011). River water
326 temperatures were taken as 3-day running averages of the air observed temperature. We
327 initialized the model using observed water temperature profiles throughout the lake from a
328 spring-summer survey (ECCC); whereas the initial velocity field was quiescent ('cold' start).
329 Spin-up of this shallow wind driven system should be within a 17 h inertial period (Valipour et
330 al., 2015b). In the 2008 model run, the observed TSS concentrations were specified from river
331 loading (León et al., 2011) and pumped water samples collected at multiple stations were used as
332 validation data and initial conditions (Bouffard et al., 2013). The models were run for 100 days
333 in 2008 (days 203-303), and 157 days in 2009 (days 118-275), with a 5 min timestep, to satisfy
334 the Courant-Friedrichs-Levy condition.

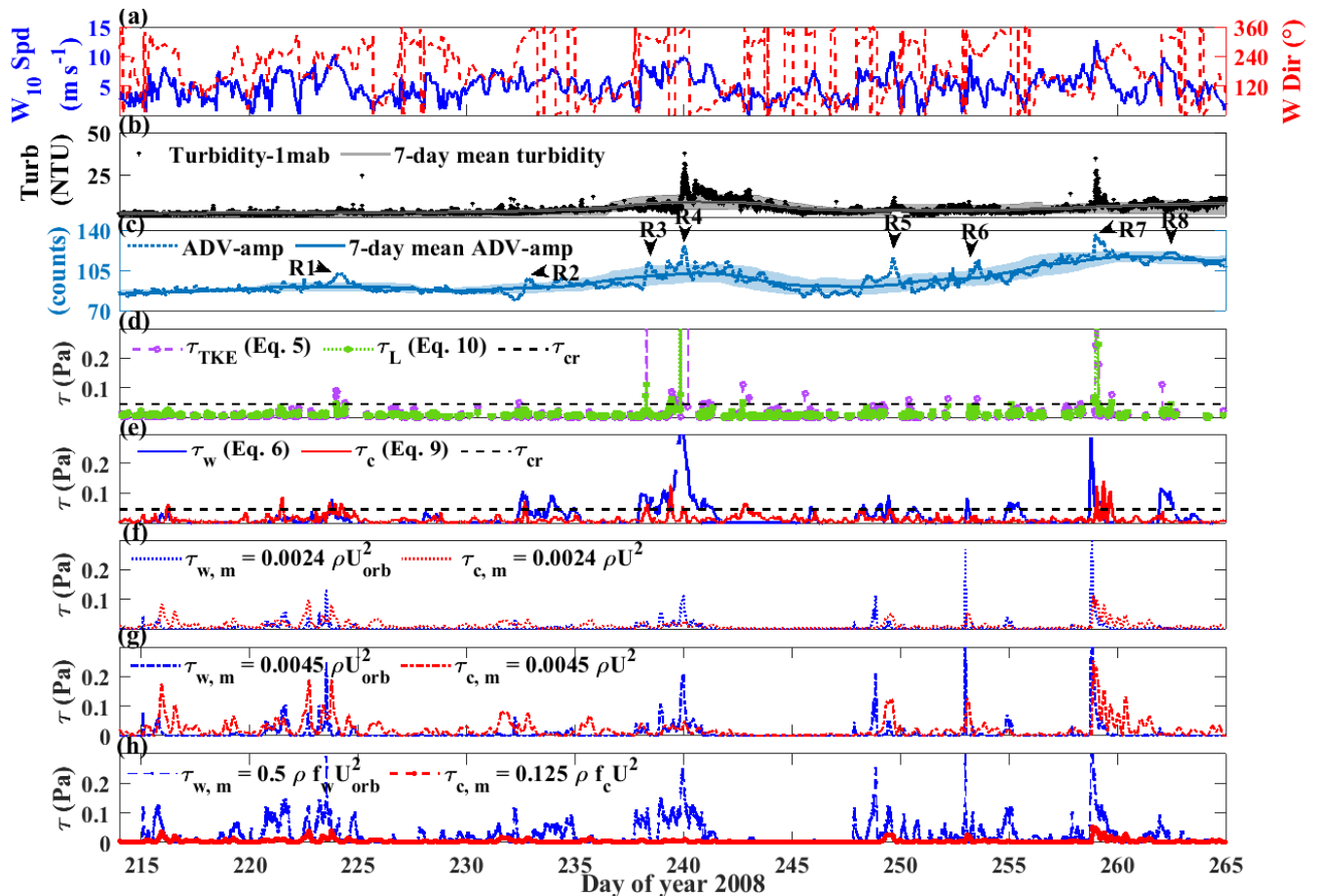
335 Sediments in the models were separated into three classes: river loads (SS_R , $d_{50} = 3 \mu\text{m}$;
336 (Fukuda and Lick, 1980) and lakebed (SS_{B1} , $d_{50} = 1 \mu\text{m}$; SS_{B2} , $d_{50} = 10 \mu\text{m}$; Lick et al., 1994).
337 SS_{B1} represented clay-like superficial (nepheloid) sediments (Lick et al., 1994), whereas SS_{B2}
338 represented the silt-like sediments below (Hawley and Eadie, 2007; Valipour et al., 2017). The
339 lakebed sediment classes were proportioned at 20% (clay) and 75% (silt), according to
340 observations from the PONAR grabs (J. D. Ackerman, personal communication).

341 Results from ELCD and AEM3D were quantitatively compared to the observation-based
342 bottom stress parameterizations using the percent bias (P_{bias}), Pearson correlation coefficient (R),
343 and the root-mean-square error ($RMSE$).

344 **3. Results**

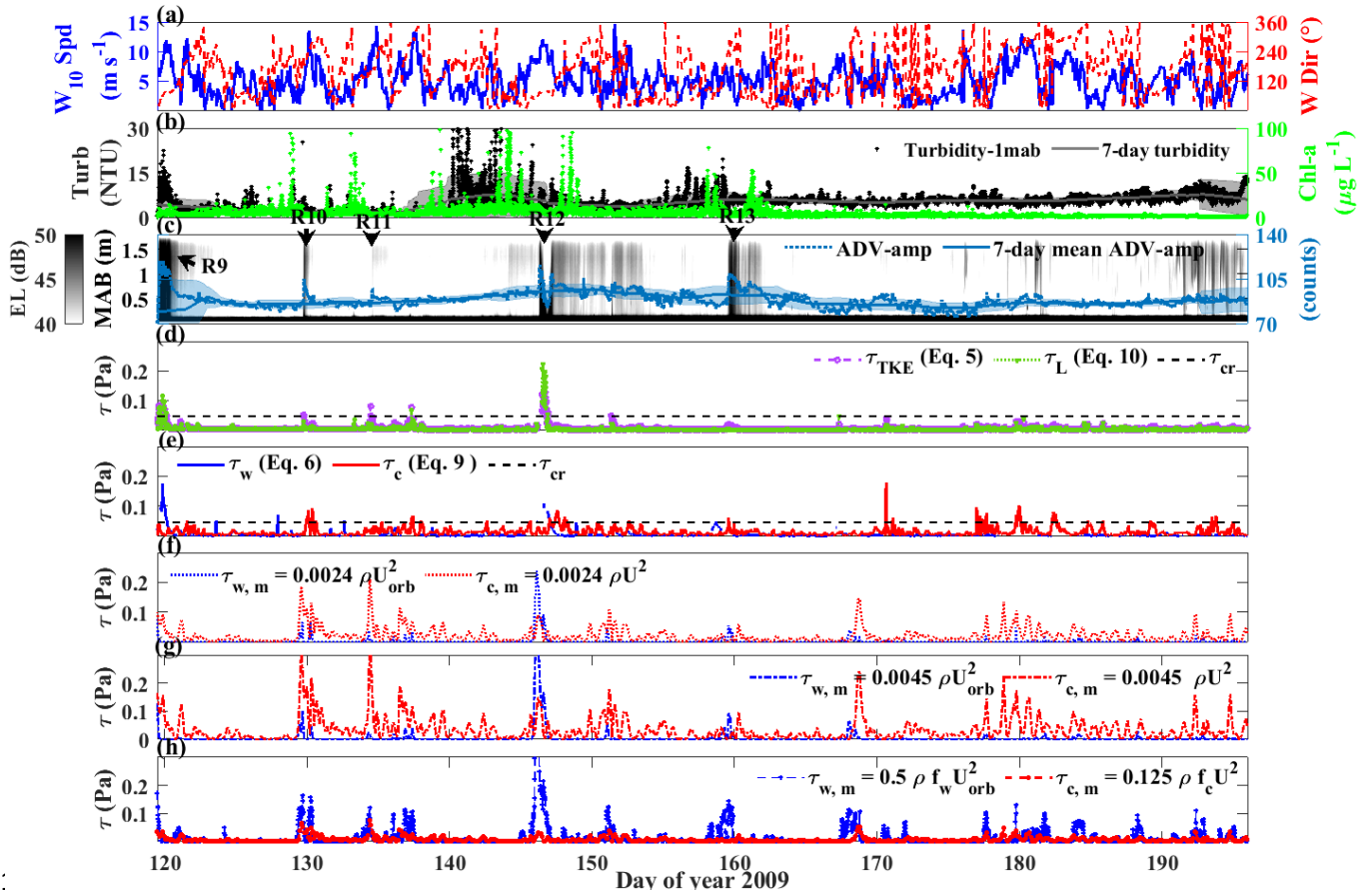
345 **3.1 Prediction of resuspension from observed τ_b**

346 In the spring and summer, settling of algae (Paerl et al., 2011; Modis, NOAA Coastwatch-
 347 Great Lakes) contributed to some turbidity peaks consistent with high fluorescence (*Chl-a*)
 348 during the first deployment period (days 119-195) of 2009. We followed Valipour et al. (2017),
 349 who used the Medium Resolution Imaging Spectrometer (MERIS) to separate turbidity peaks
 350 due to resuspension from those due to high algal biomass (Sta. 341, days 226, 236, 245; Fig. 4b).
 351 We then identified twenty-three sediment resuspension events (Fig. 2-4; R1-23) from turbidity,
 352 ADV-amp and ADCP echo data. All three indicators showed resuspension during several
 353 especially intense events (R1, 3, 4, 7, 9, 12, 13, 21-23).

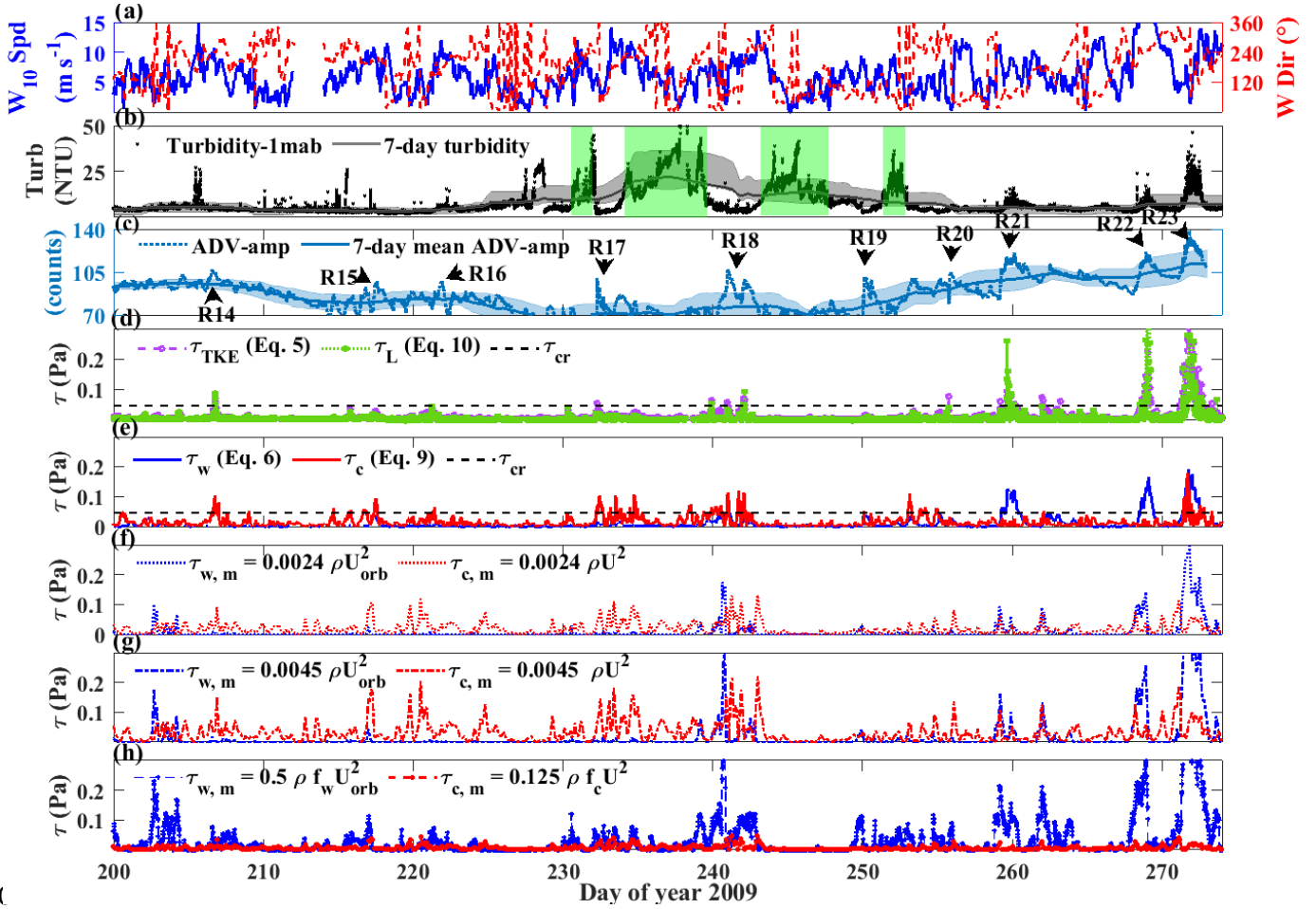


354 **Fig. 2.** Time-series at Sta. 341 for 2008 (a) wind speed (blue line; left y-axis) and direction (red dashed line; right y-
 355

356 axis) at 10 m above water surface, (b) turbidity at 1.5 mab from XR-620 (black stars) and its 7-day moving mean
 357 (grey line) and 7-day standard deviation (grey shading), (c) ADV-amp at 1 mab (blue dots) and its 7-day moving
 358 mean (blue line) and 7-day standard deviation (blue shading), (d) τ_L (purple dash-dot line, Eq. 10), τ_{TKE} (green
 359 dash-dot line, Eq. 5) and critical value for resuspension ($\tau_{cr}=0.045$ Pa; black dashed line), (e) τ_w (blue line, Eq. 6),
 360 τ_c (red line, Eq. 9) and τ_{cr} , (f-h) Modeled $\tau_{c,m}$ and $\tau_{w,m}$ based on varying C_D and algorithms.



36: **Fig. 3.** Time-series at Sta. 341 for first deployment in 2009 (a) wind speed (blue line; left y-axis) and direction (red
 362 dashed line; right y-axis) at 10 m above water surface, (b) turbidity at 1.5 mab from XR-620 (black stars) and its 7-
 363 day moving mean (grey line) and standard deviation (grey shading) (left y-axis). Green stars are *Chl-a* concentration
 364 at 5 mab from XR-420 (right y-axis), (c) ADV-amp at 1 mab (blue dots) and its 7-day moving mean (blue line) and
 365 standard deviation (blue shading). Color bar shows the ADCP echo level, (d) τ_L (purple dash-dot line, Eq. 10), τ_{TKE}
 366 (green dash-dot line, Eq. 5) and τ_{cr} (black dashed line), (e) τ_w (blue line, Eq. 6), τ_c (red line, Eq. 9) and τ_{cr} , (f-g)
 367 Modeled $\tau_{c,m}$ and $\tau_{w,m}$ based on the algorithms in AEM3D with varying C_D (h) Modeled $\tau_{c,m}$ and $\tau_{w,m}$ based on
 368 the algorithms in ELCD.



370

371 **Fig. 4.** Time-series at Sta. 341 for second deployment in 2009 (a) wind speed (blue line; left y-axis) and direction
 372 (red dashed line; right y-axis) at 10 m above water surface, (b) turbidity at 1.5 mab from XR-620 (black stars) and
 373 its 7-day moving mean (grey line) and standard deviation (grey shading), and green shading indicates the high
 374 turbidity from algae (Paerl et al., 2011), (c) ADV-amp at 1 mab (blue dots) and its 7-day moving mean (blue line)
 375 and standard deviation (blue shading), (d) τ_L (purple dash-dot line, Eq. 10), τ_{TKE} (green dash-dot line, Eq. 5) and
 376 τ_{cr} (black dashed line), (e) τ_w (blue line, Eq. 6), τ_c (red line, Eq. 9) and τ_{cr} , (f-g) Modeled $\tau_{c,m}$ and $\tau_{w,m}$ based on
 377 the algorithms in AEM3D with varying C_D (h) Modeled $\tau_{c,m}$ and $\tau_{w,m}$ based on the algorithms in ELCD.

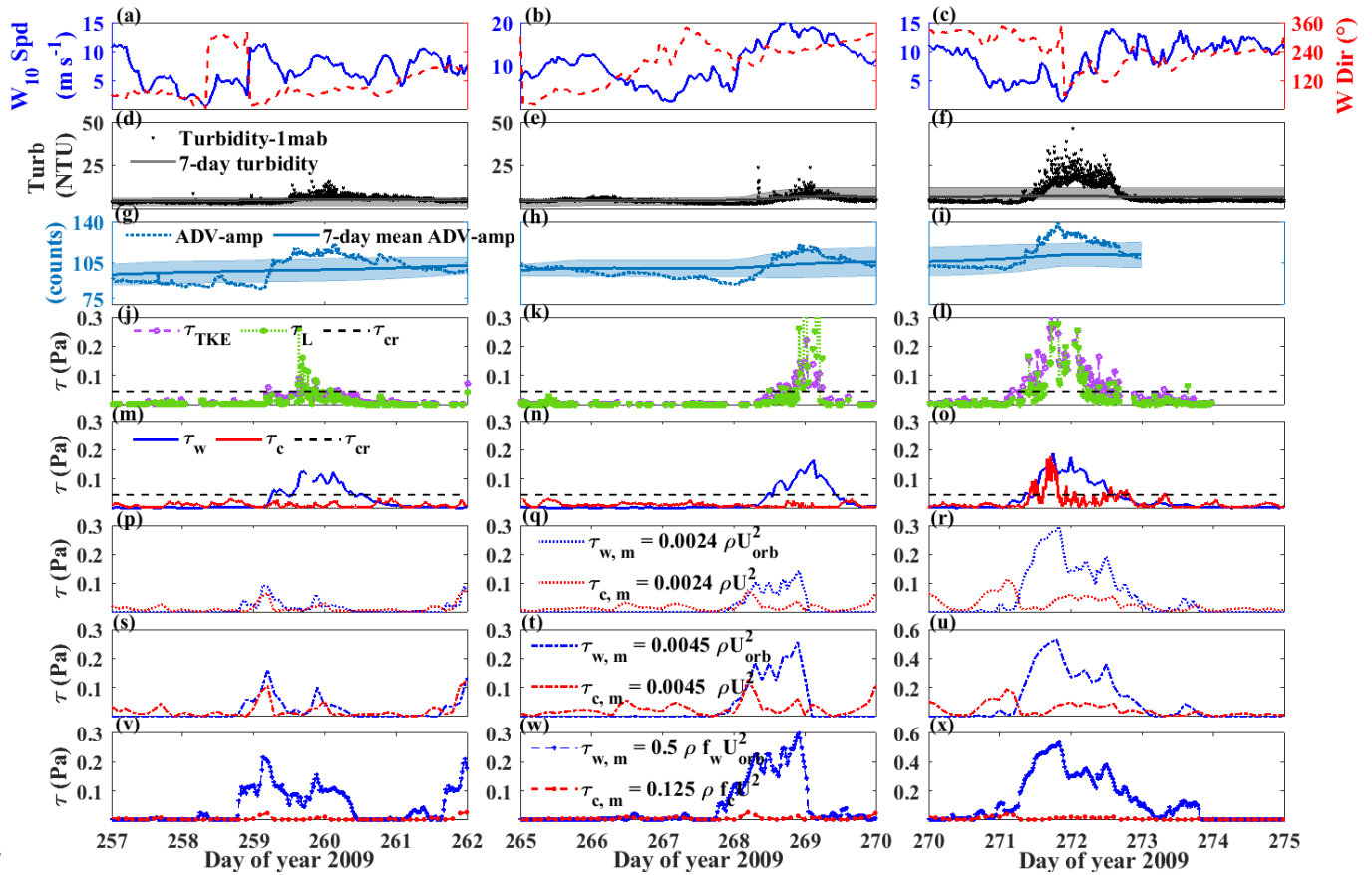
378 The four parameterizations (Eq. 5, 6, 9, and 10) were applied to compute τ_b from the
 379 observed data and compared with τ_{cr} to predict the occurrence of resuspension events. During
 380 intensive resuspension events, $\tau_b = \tau_w + \tau_c$, τ_L , τ_{TKE} were qualitatively consistent, with spikes
 381 of different magnitudes (Fig. 2b-c, 3b-c, 4b-c; R1, 3, 4, 7, 9, 12, 14, 18, and 21-23).

382 Strong wind events created significantly increased τ_w , leading to surface wave-dominated
 383 resuspension events (e.g., R21 and R22; Fig. 5). During these events, high wind speeds (> 10 m

384 s^{-1}) were observed (see also Hawley and Eadie 2007). Given that wave orbitals penetrating to
385 the lakebed can form turbulent eddies, τ_L and τ_{TKE} often showed remarkable increases (> 0.2 Pa)
386 during surface wave-dominated resuspension.

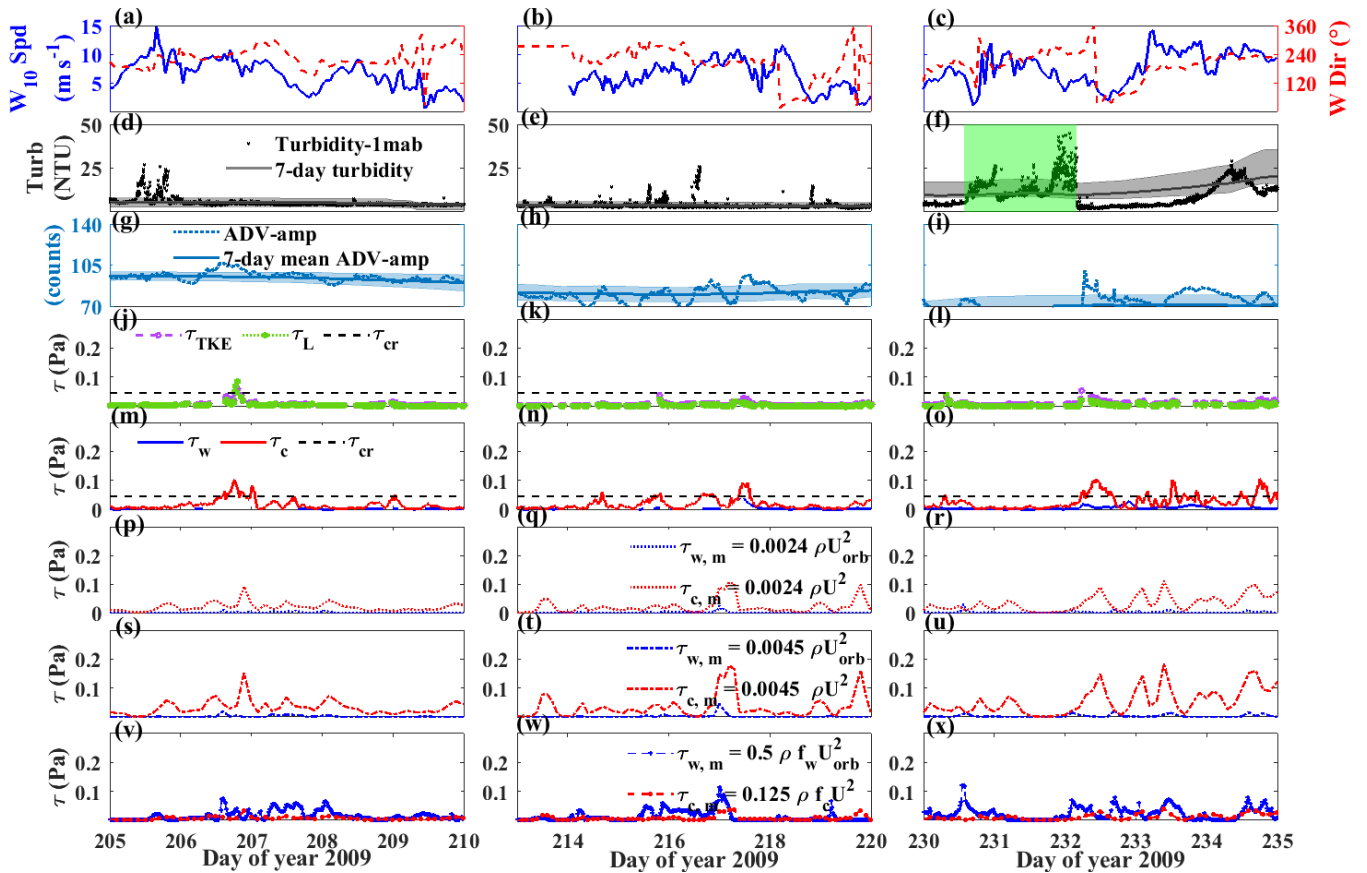
387 Bottom current-dominated resuspension events were also observed (e.g., R14-17; Fig. 6)
388 with increased τ_c exceeding τ_{cr} . Both τ_L and τ_{TKE} were elevated (>0.045 Pa), indicating the
389 turbulent eddies formed due to bottom friction. Compared to surface wave-dominated
390 resuspension, R14–17 exhibited a more gradual increase in τ_L and τ_{TKE} (< 0.1 Pa), indicating
391 bottom currents were less efficient in triggering turbulent bursts compared to wave orbitals.

392 Most resuspension events were not induced by a single mechanism but resulted from
393 combined effects of surface waves and mean currents. Storm-induced mean currents have been
394 observed after strong wind events in Lake Erie (Lick et al., 1994; Beletsky et al., 1999; Hawley
395 and Eadie, 2007), leading to increased τ_c and generating resuspension (e.g., R1-5, 7, 9, 10, 12,
396 18, 19, 20, 23). However, τ_w or τ_c acting in isolation did not always reproduce the exact timing
397 of strong resuspension, rather τ_L and τ_{TKE} corresponded with peaks of ADV-amp and turbidity
398 more accurately (R7, R10, and R12; Fig. 7). This was in agreement with oceanic (Bluteau et al.,
399 2016) and laboratory (Aghsaei and Boegman, 2015) data, showing strong bottom drag to drive
400 bedload transport, with turbulent bursts required to lift sediment into the water column. For
401 example, during day 146 in 2009 (R12) wind-driven surface wave orbitals impinged on the
402 lakebed, generating turbulence ($\tau_w \sim 0.1$ Pa, τ_L and $\tau_{TKE} \sim 0.2$ Pa; Fig. 7) and triggering
403 significant peaks in ADV-amp ADCP echo level, and turbidity. This was followed by barotropic
404 currents from basin-scale seiche events that formed as the wind subsided (Beletsky et al., 1999;
405 Valipour et al., 2015b) and generated $\tau_c > \tau_{cr}$ on day 147, leading to another peak in these three
406 resuspension indicators.



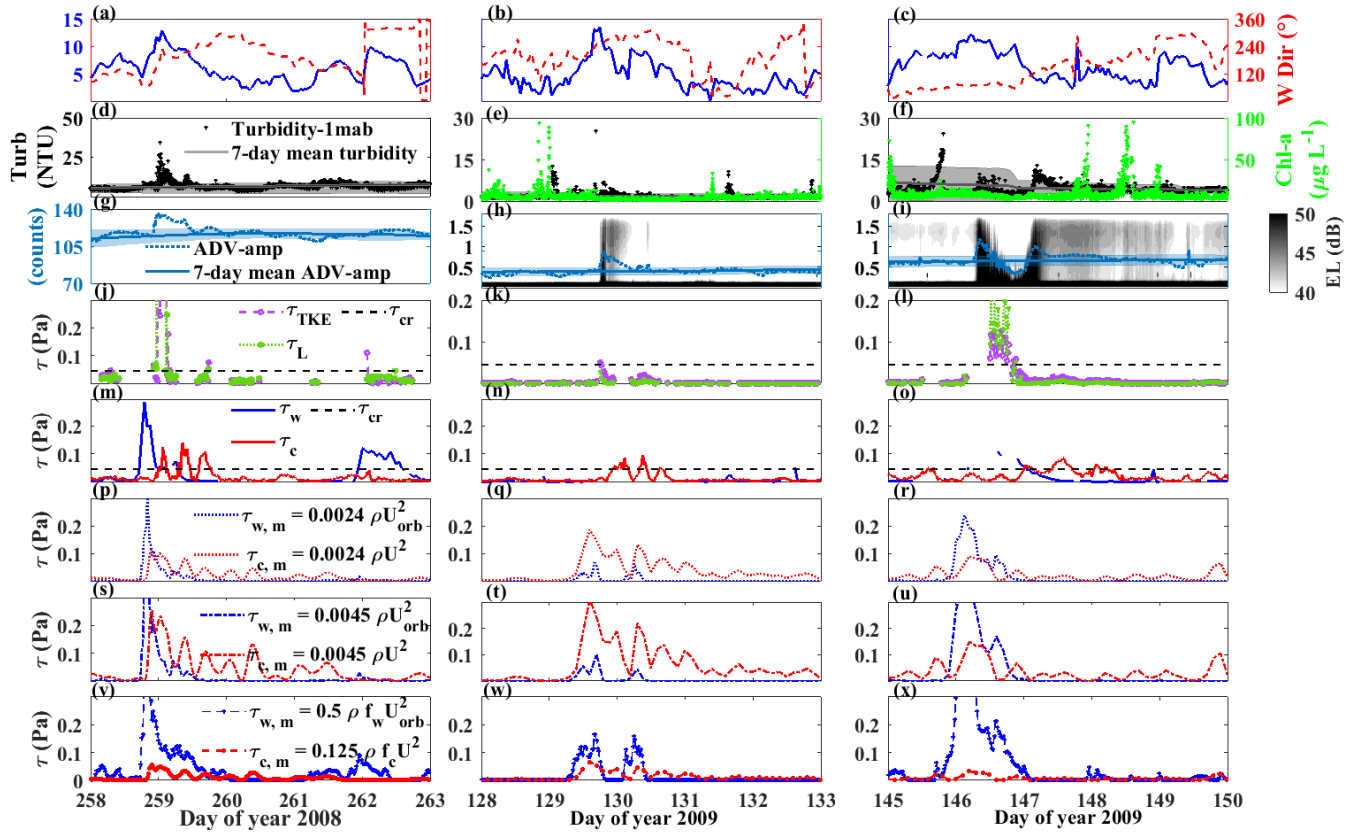
407

408 **Fig. 5** Details of resuspension events R21-23 in Fig. 4. Time-series at Sta. 341 of (a-c) wind speed (blue lines; left
 409 y-axis) and direction (red dashed lines; right y-axis) at 10 m above water surface, (b-f) turbidity at 1.5 mab from
 410 XR-620 (black stars) and its 7-day moving mean (grey line) and standard deviation (grey shading), (g-i) ADV-amp
 411 at 1 mab (right y-axis), and its 7-day moving mean (blue line) and standard deviation (blue shading), (j-l) show τ_{TKE}
 412 (τ_{TKE} (purple dash-dot line, Eq. 5) and τ_L (green dash-dot line, Eq. 10) based on turbulent velocity from ADV, and *in situ*
 413 critical value for resuspension $\tau_{cr} = 0.045$ Pa, (m-o) τ_w (blue line, Eq. 6) based NDBC station 45005, τ_c (red line,
 414 Eq. 9) based on mean current velocity from ADV, and τ_{cr} (black dashed line), (p-r) AEM3D output $\tau_{w,m}$ (blue
 415 dotted line) and $\tau_{c,m}$ (red dotted line) used $C_D = 0.0024$, (s-u) AEM3D output $\tau_{w,m}$ (blue dashed line) and $\tau_{c,m}$ (red
 416 dashed line) used $C_D = 0.0045$; and (v-x) are ELCD output $\tau_{w,m}$ (blue dashed line) and $\tau_{c,m}$ (red dashed line).



417

418 **Fig. 6** Details of resuspension events R14, 15, 17 in Fig. 3. Time-series at Sta. 341 of (a-c) wind speed (blue lines;
 419 left y-axis) and direction (red dashed lines; right y-axis) at 10 m above water surface, (b-f) turbidity at 1.5 mab from
 420 XR-620 (black stars) and its 7-day moving mean (grey line) and standard deviation (grey shading), green shading
 421 indicates the high turbidity from algae (Paerl et al., 2011), (g-i) ADV-amp at 1 mab (right y-axis), and its 7-day
 422 moving mean (blue line) and standard deviation (blue shading), (j-l) show τ_{TKE} (purple dash-dot line, Eq. 5) and τ_L
 423 (green dash-dot line, Eq. 10) based on turbulent velocity from ADV, and *in situ* critical value for resuspension $\tau_{cr} =$
 424 0.045 Pa, (m-o) τ_w (blue line, Eq. 6) based NDBC station 45005, τ_c (red line, Eq. 9) based on mean current velocity
 425 from ADV, and τ_{cr} (black dashed line), (p-r) AEM3D output $\tau_{w,m}$ (blue dotted line) and $\tau_{c,m}$ (red dotted line) used
 426 $C_D = 0.0024$; (s-u) AEM3D output $\tau_{w,m}$ (blue dashed line) and $\tau_{c,m}$ (red dashed line) used $C_D = 0.0045$, and (v-x)
 427 are ELCD output $\tau_{w,m}$ (blue dashed line) and $\tau_{c,m}$ (red dashed line).



428

429 **Fig. 7** Details of resuspension events R7, 10, 12 in Fig. 2, 3. Time-series at Sta. 341 of (a-c) wind speed (blue lines;
 430 left y-axis) and direction (red dashed lines; right y-axis) at 10 m above water surface, (b-f) turbidity at 1.5 mab from
 431 XR-620 (black stars) and its 7-day moving mean (grey line) and standard deviation (grey shading), and Chl-a
 432 concentration at 5 mab from XR-420 (right y-axis), (g-i) ADV-amp at 1 mab (right y-axis), its 7-day moving mean
 433 (blue line) and standard deviation (blue shading), and colorbar shows the ADCP echo level; (j-l) show τ_{TKE} (purple
 434 dash-dot line, Eq. 5) and τ_L (green dash-dot line, Eq. 10) based on turbulent velocity from ADV, and *in situ* critical
 435 value for resuspension ($\tau_{cr} = 0.045$ Pa; black dashed line); (m-o) τ_w (blue line, Eq. 6) based NDBC station 45005,
 436 τ_c (red line, Eq. 9) based on mean current velocity from ADV, and τ_{cr} (black dashed line); (p-r) AEM3D output
 437 $\tau_{w,m}$ (blue dotted line) and $\tau_{c,m}$ (red dotted line) used $C_D = 0.0024$; (s-u) AEM3D output $\tau_{w,m}$ (blue dashed line)
 438 and $\tau_{c,m}$ (red dashed line) used $C_D = 0.0045$; and (v-x) are ELCD output $\tau_{w,m}$ (blue dashed line) and $\tau_{c,m}$ (red
 439 dashed line).

440

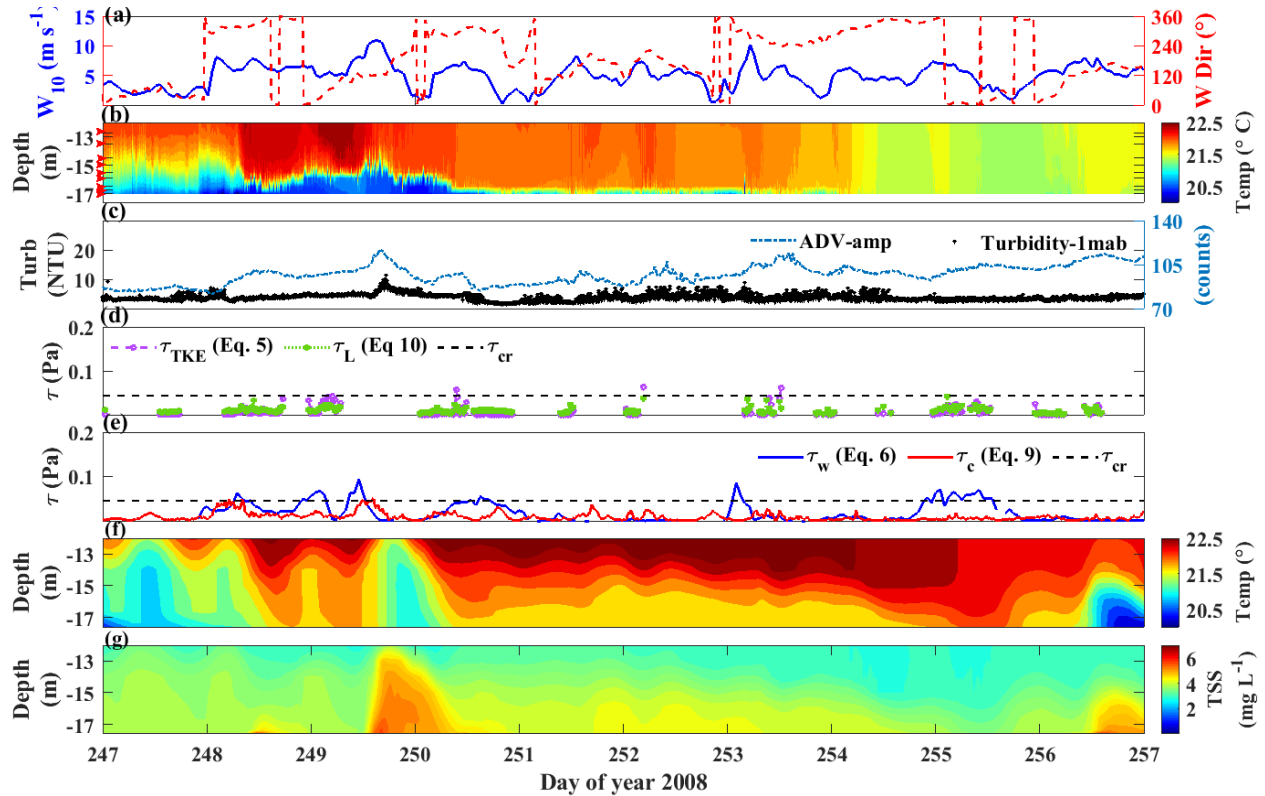
We have investigated the ability to parameterize resuspension by wave-orbital and seiche-
 441 induced mean currents; however, $\tau_b = \tau_c + \tau_w$ is not expected to be able to parameterize
 442 resuspension resulting from near-bed turbulent events forced by other processes (e.g., convection,
 443 Kelvin-Helmholtz billows). For example, Valipour et al. (2017) suggested that degeneration of
 444 Kelvin-Helmholtz billows could resuspend bottom material, when the induced turbulence

445 penetrated to the bed (see also Hawley et al., 2004; Austin, 2013). These events could only be
446 captured by τ_L and τ_{TKE} , because τ_c utilizes time-averaged mean currents that filter turbulence.
447 Here, we test the observational parameterizations for this type of event.

448 After a wind event on day 249 (Fig. 8), the thermocline, acting as a waveguide for high-
449 frequency internal waves (HFIW), impinged upon the lakebed (days 250-254). The HFIWs had
450 a period ~ 17 min (Valipour et al., 2017), which was close to the Brunt-Väisälä frequency and
451 much less than the ~ 17 hr inertial period; indicating they likely result from shear instability
452 across the thermocline (Bouffard et al., 2012; Boegman et al., 2003). During this 10-day event,
453 $\tau_b = \tau_c + \tau_w > \tau_{cr}$ on days 248-9 (Fig. 8e), corresponding to an increase of ADV-amp and
454 turbidity (R6). This was followed by spikes in τ_L and τ_{TKE} above τ_{cr} on days 252 and 253.5,
455 corresponding to peaks in ADV-amp and high turbidity (Fig. 8d). At these times, when τ_w and τ_c
456 were close to zero, HFIWs were carried on the near-bed thermocline (Fig. 8b); because the
457 peaks in τ_L and τ_{TKE} matched peaks in ADV-amp and turbidity, this suggested the mechanism
458 triggering near-bed high turbidity could be turbulent eddies generated by collapse of Kelvin-
459 Helmholtz billows as the HFIWs degenerate (Fig. 8c, d). Compared to resuspension induced by
460 τ_c or τ_w , the intensity of resuspension generated during HFIWs was lower. Both turbidity and
461 ADV-amp were elevated for several days, showing that turbulent eddies, generated when the
462 thermocline impinged on the lakebed, created an oscillatory nepheloid-type layer in the
463 hypolimnion. In this example, τ_L and τ_{TKE} provided a better estimate of sediment resuspension.

464 Overall, the observations spanning the summer of 2008 and spring-fall of 2009 revealed that
465 τ_L and τ_{TKE} showed peaks during resuspension triggered by surface wave orbitals, mean bottom
466 currents and HFIWs. The magnitude of the stress was relatively higher in magnitude during
467 resuspension involving a contribution from surface waves (e.g., R7, 12, 21-23; Fig. 5, 7) and

468 relatively lower in magnitude during resuspension from mean bottom currents or HFIWs (e.g.,
 469 R10, 14-17; Fig. 6, 7). Moreover, $\tau_b = \tau_w + \tau_c > \tau_{cr}$ was able to predict all resuspension
 470 events induced by wave orbitals (R8, 21, 22), increased bottom currents (R13, 14-17) and a
 471 combination of these two mechanisms (R1-5, 7, 9, 10, 12, 18, 19, 20, 23).



472
 473 **Fig. 8** Details of resuspension events R6 in Fig. 2. Time-series at Sta. 341 of 2008 (a) wind speed (left y-axis) and
 474 direction (right y-axis) at 10 m above water surface, (b) temperature contours from TR-1060 temperature loggers,
 475 red arrows show vertical locations of temperature loggers, (c) turbidity at 1.5 mab from XR-620 (left y-axis), and
 476 ADV-amp at 1 mab (right y-axis); (d) and (e) show τ_L (green dash-dot line, Eq. 10), τ_{TKE} (purple dash-dot line, Eq.
 477 5), τ_w (blue line, Eq. 6), τ_c (red line, Eq. 9) based on observed data and τ_{cr} (black dashed line); (f) and (g) are ELCD
 478 output of temperature and TSS concentration at Sta. 341, respectively.

479 3.2 Prediction of resuspension from RANS modeled τ_b

480 Here, we compare the observed bottom stress, required for resuspension, against those
 481 simulated by the models. ELCD qualitatively captured the occurrence of strong resuspension
 482 events induced by both bottom currents and surface waves in 2008 and 2009 (Lin et al., 2021b)

483 (Supporting Information, Fig. S4, S5). However, as calibrated against the turbidity data, the
484 threshold for sediment resuspension in ELCD (0.01- 0.025 Pa) was lower than the observed *in*
485 *situ* time-averaged threshold ($\tau_{cr} = 0.045$ Pa).

486 The present magnitude of $\tau_{c,m}$, parameterized based on the Reynold-averaged current speed
487 (Eq. 14), was much less than the observed τ_c (Figs. 3-5 e, h). Because wave stresses were
488 overestimated with ELCD ($\tau_{w,m} > \tau_w$; Figs. 3-5 e, h), having $\tau_{c,m} \ll \tau_{w,m}$ creates problems
489 specifying τ_{cr} within the modelling framework. Unrealistic setting of τ_{cr} , to capture current-
490 induced resuspension, will cause ELCD to respond excessively to surface wave forcing, and
491 overestimate the contribution of surface waves to resuspension (e.g., R14 - R17; Fig. 2-4).
492 Adjustment of $\tau_{c,m}$ within ELCD to resuspend at an appropriate τ_{cr} , by increasing bed
493 roughness ($k_s = 2.5 d_{50}$; d_{50} is the median sediment grain size) in Eq. (14), is not possible because
494 of the effect of d_{50} on particle settling (Lin et al., 2021b).

495 The modeled U_{orb} and U_{bot} are calculated with the same algorithms in both AEM3D and ELCD
496 (Supporting Information, Fig. S4); therefore, both overestimated the peak current speeds (U_{bot} $RMSE =$
497 0.051 m s⁻¹). There were insufficient observed wave orbital velocity measurements to calculate U_{orb} error.

498 AEM3D avoids the particle settling issues in ELCD by directly employing C_D to
499 parameterize both $\tau_{w,m}$ and $\tau_{c,m}$ (Eq. 13, 15). The AEM3D-modeled bottom current velocities
500 are not sensitive to small variations of C_D (C. Dallimore, personal communication); therefore,
501 adjustment of bottom drag focused on reproducing bottom stress, rather than bottom currents.
502 Table 1 shows the comparison of parameterizations for $\tau_{w,m}$ and $\tau_{c,m}$ in AEM3D and ELCD.
503 ELCD (Eq. 6) overestimated surface wave-induced stress (Fig 3-5 e, h), with $RMSE = 0.052$ Pa
504 and $P_{bias} = 57\%$ (Table 1; $\tau_{w,m1}$). The error was less using the parameterization in AEM3D (Eq.
505 13), with $RMSE = 0.031$ Pa and $P_{bias} \sim 0$ when $C_D = 0.0024$ (Fig. 2-4 e, f).

506 The parameterization of quadratic stress in ELCD (Table 1, $\tau_{c,m1}$) gave the lowest *RMSE*,
507 but the $P_{bias} = -46\%$ showed the overall underestimation of the magnitude (Fig. 2-4 h). Given that
508 ELCD and AEM3D overestimate current speed, particularly the peak values (Fig. S4), when
509 applying the observed $C_D = 0.0045$ in Eq. 15 (Table 2, $\tau_{c,m2}$) the P_{bias} was highest (196%)
510 amongst the three parameterizations. Thus, applying the canonical $C_D = 0.0024$ in Eq. 15
511 compensated for overestimation of current speed, reproducing an appropriate magnitude for the
512 quadratic stress (Figs. 3-5 e, f). This gave $RMSE = 0.025$ Pa and the lowest P_{bias} (= 34%).

513 3.3 Turbulence-based parameterizations in RANS models

514 The inability of the models to resolve the sub-grid turbulence, may result in only a subset of
515 resuspension events being simulated, and those resulting from mean shear-free boundary
516 turbulence (Johnson and Cowen, 2020) being neglected (e.g., HFIW events). Thus, we applied
517 Eq. 11, using the modeled ε_m (Eq. 16) to assess the possibility of employing a log-law based
518 turbulence parameterization in a RANS sediment model. Here, the modeled/observed turbulence
519 may result from mean shear-free processes (e.g., convection), but the resultant stress follows log-
520 law scaling (Eq. 11). The computed $\tau_{L,m}$ was higher than the observed τ_L most of the times (Fig.
521 9) and the model was unable to capture peaks in observed τ_L . Table 1 shows the agreement
522 between $\tau_{L,m}$ and τ_L is poor ($R^2 = 0.05$). To investigate why, ε_{ID} and ε_m were compared at
523 selected periods (Supporting Information, Fig. S7), showing reasonable qualitative comparison,
524 but frequent quantitative differences of more than an order of magnitude. This was not
525 unexpected as the modeled dissipation output is the TKE remaining at the end of a timestep and,
526 therefore, is useful as a diagnostic output for the individual components in the TKE
527 parametrization (C. Dallimore, personal communication).

528 **Table 1**

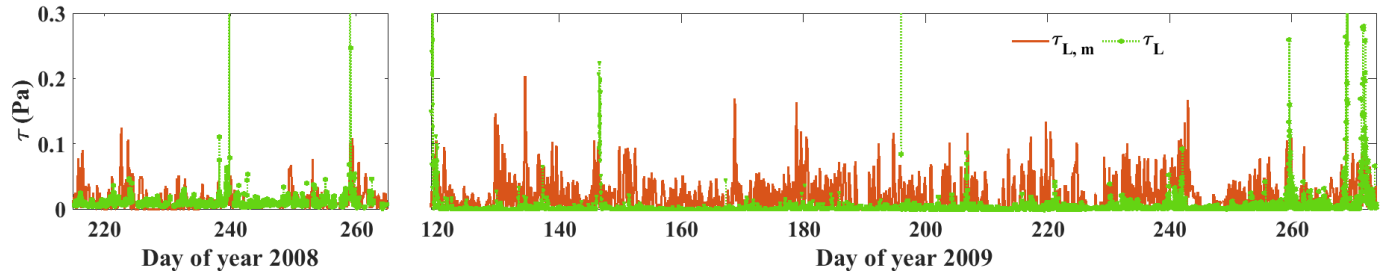
529 *Assessment of bottom stress parameterization in ELCD (denoted by m1) and AEM3D (denoted by m2, 3) models.*

	Modeled $\tau_{w,m1}$	Modeled $\tau_{w,m2}$	Modeled $\tau_{w,m3}$	Modeled $\tau_{c,m1}$	Modeled $\tau_{c,m2}$	Modeled $\tau_{c,m3}$	Modeled $\tau_{L,m}$
<i>RMSE</i>	0.052 Pa	0.042 Pa	0.031 Pa	0.017 Pa	0.047 Pa	0.025 Pa	1.7 Pa
<i>R</i> ²	0.51	0.46	0.47	0.15	0.13	0.15	0.05
<i>P</i> _{bias}	57%	-27%	-2.2%	-46%	196%	34%	80%

530 $\tau_{w,m1} = 0.5 \rho f_w U_{orb}^2$; $\tau_{w,m2} = 0.0045 \rho U_{orb}^2$; $\tau_{w,m3} = 0.0024 \rho U_{orb}^2$

531 $\tau_{c,m1} = 0.125 \rho f_c U^2$; $\tau_{c,m2} = 0.0045 \rho U^2$; $\tau_{c,m3} = 0.0024 \rho U^2$

532



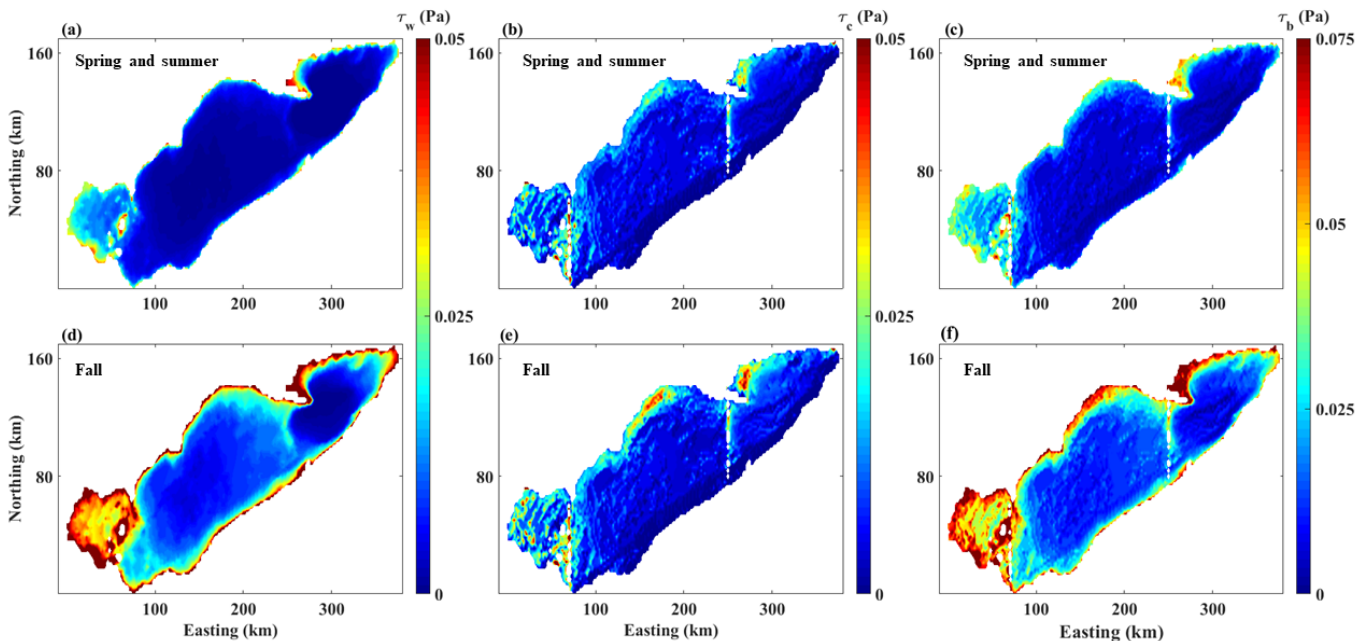
533

534 **Fig. 9** Time-series at Sta. 341 of τ_L (Eq. 11) based on ε_m (Eq. 16, orange line) and ε_{ID} (green dash-dot line).

535 Comparisons of observed and modelled turbulent dissipation are shown in Fig. S6.

536

537 **3.4 Sediment resuspension hot spots**



538

539 **Fig. 10** Mean value of AEM3D modeled $\tau_{w,m}$, $\tau_{c,m}$, and τ_b (a-c) over spring and summer (days 203 – 245 of 2008

540 and days 119- 250 of 2009), and (d-f) over fall (days 245- 303 of 2008 and days 250 – 300 of 2009).

541 To visualize variation in bottom stress throughout the basin, AEM3D simulated $\tau_{w,m}$, $\tau_{c,m}$
542 and $\tau_b = \tau_{w,m} + \tau_{c,m}$ were computed for different seasons (Fig. 10) using the AEM3D
543 parameterization based on Eqs. (13 and 15) with $C_D = 0.0024$. Resuspension hot spots were
544 identified as sites where $\tau_b = \tau_{w,m} + \tau_{c,m}$ exceeded $\tau_{cr} = 0.045$ Pa . In general, both $\tau_{w,m}$ and
545 $\tau_{c,m}$ increased in fall when storms are more prevalent on the lake.

546 The effect of surface wave orbitals decreased with increasing water depth, with the western
547 basin and littoral zones having the highest $\tau_{w,m}$. The area of modeled surface wave-induced
548 resuspension hot-spots increased from 80 km² before fall turn over to 2592 km² after fall
549 turnover (Fig. 10a, d) due to the more frequent storms (Fig. 2-4 a). The current-induced
550 resuspension hot-spots were often associated with bottom topography (e.g., the Point Pelee to
551 Sandusky island chain and the Pennsylvania Ridge; Fig. 10b, e) and were otherwise sporadically
552 distributed in the western basin and along the north shore of the central and eastern basins. The
553 area of hot-spots increased from 84 km² before fall turnover to 168 km² after fall turnover (Fig.
554 10b, e). During the spring and summer, most of the current-induced resuspension was driven by
555 wind-energized seiche events and baroclinic currents (e.g., Hawley, 2004; Rao et al., 2008;
556 Valipour et al., 2017). Combining wave-induced and current-induced stresses, the total area of
557 resuspension hot-spots was 1920 km² in spring and summer and 5196 km² in fall, being
558 concentrated in the western basin, and the northern shoreline of the central and eastern basins
559 (Fig. 10c, f).

560 **4. Discussion**

561 **4.1 Comparison of algorithms in commonly applied hydrodynamic models**

562 The AEM3D and ELCD bottom stress parameterizations are discussed with reference to the
 563 parameterizations in other commonly-applied hydrodynamic models, specifically FVCOM-SED
 564 and Delft3D (Table 2).

565 **Table 2**

566 *Parameterizations for τ_c in different sediment models. The equations in column 2 were solved using parameters*
 567 *characteristic to Lake Erie (column 4).*

Method	τ_c equation		d_{50} (m)	τ_c (using parameters in Lake Erie)
<i>In situ</i> observation	$\rho^* C_D U^2$		10^{-5}	$4.5U^2 (C_D = 4.5 \times 10^{-3})$
FVCOM-SED	$\rho \max \left[\frac{\kappa^2}{\ln(\frac{\Delta z_{bot}}{z_o^\ddagger})^2}, 0.0025 \right] U_{bot}^2$		10^{-5}	$\max[0.00082, 0.0025] \rho U^2$ $= 2.5U_{bot}^2$
Delft3D	2D flow	$\rho \frac{g}{(18 \log_{10}(\frac{12h^\#}{30z_o^\ddagger}))^2} U_{bot}^2$ (White Colebrook)	10^{-5}	$0.64U_{bot}^2$
		$\rho \frac{g}{(\frac{\sqrt{h^\#}}{n^\dagger})^2} U_{bot}^2$ (Manning)	10^{-5}	$3849n^{\dagger 2} U_{bot}^2 = 0.23U_{bot}^2$
	3D flow	$\rho \frac{\kappa^2}{\ln(1 + \frac{\Delta z_{bot}}{2z_o^\ddagger})^2} U_{bot}^2$	10^{-5}	$0.9U_{bot}^2$
ELCD	$\rho \frac{0.24}{[\log(\frac{12 \Delta z_{bot}}{k_s^*})]^2} U_{bot}^2$		10^{-5}	$0.97U_{bot}^2$
AEM3D	$\rho C_D U_{bot}^2$		10^{-5}	$4.5U_{bot}^2 (C_D= 0.0045)$ $2.4U_{bot}^2 (C_D= 0.0024)$

- * ρ Water density = 1000 kg m⁻³
- * $\Delta z_{bot} = 1$ m The thickness of the bottom layer in the models
- # $h = 16.5$ m The depth of model output current velocities
- † n User-defind manning coefficient. Theoretically, $n = 0.045(2.5 d_{50})^{1/6}$ (van Rijn, 1993).
- ‡ z_o Roughness height of the lakebed (i.e., zero velocity level) [m]: $z_o = 0.083 d_{50}$
- * k_s bed roughness, $k_s = 30 z_o$ [m]. Several relations between k_s and bottom sediment grain size have been proposed, with one of the most widely used being: $k_s = 2.5 d_{50}$.

569 ELCD, FVCOM-SED and Delft3D all use logarithmic scaling for C_D based on k_s or z_o ,
570 which are both associated with bed roughness (Table 2). In RANS models, the resolution of the
571 bathymetry is insufficient to resolve bedforms, which are difficult to measure, and consequently
572 sediment grain size is employed to calculate C_D (Table 2). As a result, C_D in these models will
573 be smaller than *in situ* observations (0.0045), which account for the effects of bottom
574 morphometry on drag. To adjust $\tau_{c,m}$ to become equivalent to the *in situ* τ_c , d_{50} (when involved
575 into the calculation of τ_c ; e.g., in ELCD or FVCOM-SED) should be set to 0.03 m, which is not
576 realistic. To alleviate this issue, FVCOM-SED sets a minimum $C_D = 0.0025$ (close to the
577 canonical value of 0.0024), bringing $\tau_{c,m}$ in FVCOM-SED closest to the observed values among
578 these three models (Table 2; Morales-Marin et al., 2018; Niu et al., 2018). Similarly, Hu et al.
579 (2009) applied the DELft3D 2D flow $\tau_{c,m}$ but set the Manning coefficient independently of d_{50}
580 (Table 2), so the model could correctly reproduce sediment resuspension using a literature-based
581 τ_{cr} . From Table 2, the difference in parameterizations is reduced to the constant in front of U_{bot}^2 .
582 Given that models tend to overestimated bottom current speed (Fig. S4), the constant not only
583 embodies bottom drag, but also adjusts for errors in hydrodynamic model output. For example, to
584 parameterize resuspension with $U > U_{bot}$ we may use $2.4U_{bot}^2 \approx 4.5U^2$. This suggests the optimal
585 C_D in the model can be computed from the observed value and ratio of observed to modelled
586 velocities as $C_D^{model} = C_D^{obs} \cdot (U^2/U_{bot}^2) = (4.5 \times 10^{-3})(2.4/4.5) = 2.4 \times 10^{-3}$.

587 The ELCD results in 2008 showed that (i.e., $\tau_{w,m}$) played a dominant role in the west
588 central basin of Lake Erie during intense storm events (Valipour et al., 2017; Lin et al., 2021b).
589 But Morales-Marin et al. (2018), who applied FVCOM-SED, modeled a much larger relative
590 proportion of the lakebed to be potentially resuspended by currents during extreme wind events
591 in an upland shallow lake in north Wales (UK). One explanation for this discrepancy is that

592 western Lake Erie has a longer fetch and so can develop stronger surface waves over its shallow
593 water depth. Another possible reason is the underestimation of the contribution from currents
594 because of the inappropriate algorithms in ELCD. Thus, by applying AEM3D with Eq. 15, the
595 magnitude of the modeled stress was closer to the observed value (Fig. 2-4 e, f, g), and the
596 relative contributions of from bottom currents were comparable to those from surface waves
597 during storms (e.g., R1, 13, 18; Fig. 2-4) in west central Lake Erie (Sta. 341). However, the
598 shallow Lake Erie morphology results in strong surface waves during intense storm events (e.g.,
599 R23; Fig. 4) dominating the overall resuspension.

600 From these comparisons, the core concept of the $\tau_{c,m}$ parameterization is determination of
601 the constant before U_{bot}^2 . Thus, we summarized two ways to parameterize $\tau_{c,m}$ in RANS models.
602 The first is to apply an *in situ* or literature-based canonical C_D value, if available, to Eq. 15
603 (Soulby et al., 1994; Zulberti et al., 2018) and adjust C_D to account for inaccuracy in modelling
604 currents, especially the peak values (Fig. S4). The second option is parameterization like
605 FVCOM-SED, which chooses the maximum value between the logarithmic derived C_D and the
606 user-defined minimum C_D ; this option requires knowledge of bed roughness z_o in the model.

607 **4.2 Parameterization based on near-bed turbulence**

608 The τ_{cr} defined by existing threshold models is most often determined by flume
609 experiments using mean current velocity profiles (Shields, 1936; Soulsby et al., 1997). However,
610 on larger scales and in more complex systems (e.g., shallow marine environments and large
611 lakes), the threshold could be reduced because of the enhanced intensity of intermittent turbulent
612 events (Salim et al., 2018; Yang et al., 2016), including resuspension from mean shear-free
613 turbulence (Johnson and Cowen, 2020). Therefore, parameterizing τ_b from time-averaged
614 current speeds is not always appropriate for modelling the bottom nepheloid layers in the

615 presence of turbulent bursting events (Bourgault et al., 2014; Aghsaee and Boegman, 2015),
616 including the turbid hypolimnion beneath HFIWs in this study. In these cases, τ_{TKE} and τ_L are
617 more appropriate because both methods parameterize near-bed turbulence (Eq. 5, 11).

618 Existing RANS models are unable to resolve w' , and so parameterizations using TKE are
619 unrealistic. Present algorithms for ε_m in RANS models (e.g., AEM3D) do not consider the energy
620 flux path associated with surface wave generation and breaking (e.g., Spigel et al., 1986; Hodges
621 et al., 2000), leading to overestimation of the energy flux entering the lake interior most of the
622 time (Fig. S6). Fig. 9 shows that $\tau_{L,m}$ was smaller than the observed τ_L , only when bottom
623 stresses were mainly from surface wave orbital velocities (R4, 7, 9, 12, 21-23). Therefore,
624 complete replacement of the present parameterization (Eq. 10, 14) with $\tau_{L,m}$ is not suitable for
625 shallow water systems with resuspension frequently triggered by surface waves. The
626 development of turbulence-based parameterizations should be an avenue of future work,
627 particularly for systems with intensive convective turbulence (Anderson et al., 1979; Johnson
628 and Cowen 2020), where shear-driven models are inappropriate.

629 **5. Conclusions**

630 Multiple parameterization methods for bottom stress (τ_b), including (1) sum of surface
631 wave stress and mean current (quadratic) stress ($\tau_b = \tau_w + \tau_c$; Eq. 6, 10); (2) log-law ($\tau_b = \tau_L$;
632 Eq. 11); and (3) turbulent kinetic energy ($\tau_b = \tau_{TKE}$; Eq. 5), have been assessed, based on
633 observed data and model output. For large and shallow waterbodies, bottom currents and surface
634 wave orbitals were the two major processes driving bottom sediment resuspension and $\tau_b =$
635 $\tau_w + \tau_c$ was sufficient to qualitatively predict resuspension. This model was readily calibrated
636 for sediment resuspension simulations in field-scale RANS models. Sub-grid-scale
637 hydrodynamics (HFIWs) also induced low-intensity resuspension events, when the seasonal

638 thermocline became close to the lakebed, and only τ_L and τ_{TKE} were able to capture the turbid
639 bottom layer generated by these events.

640 This study assessed different parameterizations for $\tau_{w,m}$ and $\tau_{c,m}$ in the RANS models and
641 the model parameterizations via Eq. 13 and 15 with canonical C_D showed lowest P_{bias} (34% and -
642 2.2%, respectively) when compared to parameterizations based on observed data (Eq. 6, 10). In
643 some commonly-applied hydrodynamic models, the parameterizations using logarithmic scaling
644 for C_D based on bed roughness, could potentially lead to underestimation of bottom stress. Thus,
645 usage of a constant, observed or literature-based C_D , is recommended but should be calibrated to
646 account for inaccuracies in modeled currents.

647 Using the observed ε and scaling the bottom stress according to the log-law (τ_L) captured
648 turbulence-driven resuspension events when the mean-shear was low. Although sub-grid-scale
649 turbulent fluctuations driving resuspension (e.g, w') are not reproduced in RANS models, the
650 log-law parameterization should be further tested and improved by better parameterization of ε to
651 allow for simulation of resuspension associated with localized turbulence from wave breaking or
652 convection.

653 **Data and Code Availability Statement**

654 Data and code used in this study are available at <https://doi.org/10.5281/zenodo.7391269> . The
655 Zenodo archive contains observed current, wind, and turbidity data, and scripts used to process
656 bottom shear stress, as well as model setups and outputs from AEM3D model. The AEM3D
657 executable is available for a nominal license fee from HydroNumerics
658 (<https://www.hydronumerics.com.au/> , last access: December 2022). The AEM3D source code
659 was not modified in this application but is available with permission from HydroNumerics.
660 ELCD model is not distributed anymore, but CAEDYM model is able to be coupled with

661 AEM3D to simulate the water quality. The CAEDYM executable is available within AEM3D
662 package.

663 Reference

- 664 Aghsaee, P., & Boegman, L. (2015). Experimental investigation of sediment resuspension beneath internal solitary
665 waves of depression. *Journal of Geophysical Research: Oceans*, 120(5), 3301-3314. doi:
666 10.1002/2014JC010401
- 667 Anderson, R. N., Hobart, M. A., & Langseth, M. G. (1979). Geothermal Convection Through Oceanic Crust and
668 Sediments in the Indian Ocean. *Science*, 204(4395), 828-832. doi: 10.1126/science.204.4395.828
- 669 Austin, J. (2013). Observations of near-inertial energy in Lake Superior. *Limnology and Oceanography*, 58(2), 715-
670 728. doi: 10.4319/lo.2013.58.2.0715
- 671 Bagnold, R. A. (1966). *An approach to the sediment transport problem from general physics*. Washington. US
672 government printing office.
- 673 Barua, D. K. (2005). Wave Hindcasting. In M. L. Schwartz (Ed.), *Encyclopedia of Coastal Science. Encyclopedia of*
674 *Earth Science Series*. Dordrecht: Springer.
- 675 Beletsky, D., Saylor, J. H., & Schwab, D. J. (1999). Mean Circulation in the Great Lakes. *Journal of Great Lakes*
676 *Research*, 25(1), 78-93. doi: 10.1016/S0380-1330(99)70718-5
- 677 Biron, P. M., Robson, C., Lapointe, M. F., & Gaskin, S. J. (2004). Comparing different methods of bed shear stress
678 estimates in simple and complex flow fields. *Earth Surface Processes and Landforms*, 29(11), 1403-1415.
679 doi: 10.1002/esp.1111
- 680 Bluteau, C., Smith, S., Ivey, G., Schlosser, T., & Jones, N. (2016). *Assessing the relationship between bed shear*
681 *stress estimates and observations of sediment resuspension in the ocean*. Paper presented at the 20th
682 Australasian Fluid Mechanics Conference.
- 683 Boegman, L., Imberger, J., Ivey, G. N., & Antenucci, J. P. (2003). High-frequency internal waves in large stratified
684 lakes. *Limnology and Oceanography*, 48(2), 895-919. doi: 10.4319/lo.2003.48.2.0895
- 685 Boegman, L., & Ivey, G. N. (2009). Flow separation and resuspension beneath shoaling nonlinear internal waves.
686 *Journal of Geophysical Research: Oceans*, 114(C2). doi: 10.1029/2007JC004411
- 687 Boegman, L., Loewen, M. R., Hamblin, P. F., & Culver, D. A. (2001). Application of a two-dimensional
688 hydrodynamic reservoir model to Lake Erie. *Canadian Journal of Fisheries and Aquatic Sciences*, 58(5),
689 858-869. doi:10.1139/f01-035
- 690 Boegman, L., & Stastna, M. (2019). Sediment Resuspension and Transport by Internal Solitary Waves. *Annual*
691 *Review of Fluid Mechanics*, 51(1), 129-154. doi:10.1146/annurev-fluid-122316-045049
- 692 Boudreau, B. P., & Jorgensen, B. B. (2001). *The benthic boundary layer: Transport processes and biogeochemistry*.
693 New York. Oxford University Press. Inc.
- 694 Bouffard, D., Ackerman, J. D., & Boegman, L. (2013). Factors affecting the development and dynamics of hypoxia
695 in a large shallow stratified lake: Hourly to seasonal patterns. *Water Resources Research*, 49(5), 2380-2394.
696 doi: 10.1002/wrcr.20241
- 697 Bouffard, D., Boegman, L., Ackerman, J. D., Valipour, R., & Rao, Y. R. (2014). Near-inertial wave driven dissolved
698 oxygen transfer through the thermocline of a large lake. *Journal of Great Lakes Research*, 40(2), 300-307.
699 doi: 10.1016/j.jglr.2014.03.014
- 700 Bouffard, D., Boegman, L., & Rao, Y. R. (2012). Poincaré wave-induced mixing in a large lake. *Limnology and*
701 *Oceanography*, 57(4), 1201-1216. doi: 10.4319/lo.2012.57.4.1201
- 702 Bourgault, D., Morsilli, M., Richards, C., Neumeier, U., & Kelley, D. E. (2014). Sediment resuspension and
703 nepheloid layers induced by long internal solitary waves shoaling orthogonally on uniform slopes.
704 *Continental Shelf Research*, 72, 21-33. doi: 10.1016/j.csr.2013.10.019
- 705 Bruton M.N. (1985) The effects of suspensoids on fish. In: Davies B.R., Walmsley R.D. (eds) *Perspectives in*
706 *Southern Hemisphere Limnology. Developments in Hydrobiology*, vol 28. Springer, Dordrecht. doi:
707 10.1007/978-94-009-5522-6_16
- 708 Churchill, J. H., Williams, A. J., & Ralph, E. A. (2004). Bottom stress generation and sediment transport over the
709 shelf and slope off of Lake Superior's Keweenaw peninsula. *Journal of Geophysical Research: Oceans*,
710 109(C10). doi: 10.1029/2003JC001997

711 Donohue, I., & Garcia Molinos, J. (2009). Impacts of increased sediment loads on the ecology of lakes. *Biological*
712 *Reviews*, 84(4), 517-531. doi: 10.1111/j.1469-185X.2009.00081.x

713 Fukuda, M. K., & Lick, W. (1980). The entrainment of cohesive sediments in freshwater. *Journal of Geophysical*
714 *Research: Oceans*, 85(C5), 2813-2824. doi: 10.1029/JC085iC05p02813

715 Haltuch, M. A., Berkman, P. A., & Garton, D. W. (2000). Geographic information system (GIS) analysis of
716 ecosystem invasion: Exotic mussels in Lake Erie. *Limnology and Oceanography*, 45(8), 1778-1787. doi:
717 10.4319/lo.2000.45.8.1778

718 Hawley, N., & Eadie, B. J. (2007). Observations of Sediment Transport in Lake Erie during the Winter of 2004–
719 2005. *Journal of Great Lakes Research*, 33(4), 816-827. doi: 10.3394/0380-
720 1330(2007)33[816:OOSTIL]2.0.CO;2

721 Hawley, N., Lesht, B. M., & Schwab, D. J. (2004). A comparison of observed and modeled surface waves in
722 southern Lake Michigan and the implications for models of sediment resuspension. *Journal of Geophysical*
723 *Research: Oceans*, 109(C10). doi: 10.1029/2002JC001592

724 Hawley, N., Wang, X., Brownawell, B., & Flood, R. (1996). Resuspension of Bottom Sediments in Lake Ontario
725 During the Unstratified Period, 1992–1993. *Journal of Great Lakes Research*, 22(3), 707-721. doi:
726 10.1016/S0380-1330(96)70991-7

727 Hodges, B. R., Imberger, J., Saggio, A., & Winters, K. B. (2000). Modeling basin-scale internal waves in a stratified
728 lake. *Limnology and Oceanography*, 45(7), 1603-1620. doi: 10.4319/lo.2000.45.7.1603

729 Hu, K., Ding, P., Wang, Z., Yang, S. (2009). A 2D/3D hydrodynamic and sediment transport model for the Yangtze
730 Estuary, China. *Journal of Marine Systems*, 77(1), 114-136. doi: 10.1016/j.jmarsys.2008.11.014

731 Jabbari, A., Boegman, L., & Piomelli, U. (2015). Evaluation of the inertial dissipation method within boundary
732 layers using numerical simulations. *Geophysical Research Letters*, 42(5), 1504-1511.
733 doi:10.1002/2015GL063147

734 Jabbari, A., Boegman, L., Valipour, R., Wain, D., & Bouffard, D. (2020). Dissipation of Turbulent Kinetic Energy
735 in the Oscillating Bottom Boundary Layer of a Large Shallow Lake. *Journal of Atmospheric and Oceanic*
736 *Technology*, 37(3), 517-531. doi:10.1175/jtech-d-19-0083.1

737 Jonsson, I. G. (1966). Wave Boundary Layers and Friction Factors. In *Coastal Engineering 1966* (pp. 127-148).

738 Johnson, B. A., & Cowen, E. A. (2020). Sediment suspension and bed morphology in a mean shear free turbulent
739 boundary layer. *Journal of Fluid Mechanics*, 894, A8. doi:10.1017/jfm.2020.222

740 Kim, S.-C., Friedrichs, C. T., Maa, J. P.-Y., & Wright, L. D. (2000). Estimating Bottom Stress in Tidal Boundary
741 Layer from Acoustic Doppler Velocimeter Data. *Journal of Hydraulic Engineering*, 126(6), 399-406. doi:
742 10.1061/(ASCE)0733-9429(2000)126:6(399)

743 León, L. F., Imberger, J., Smith, R. E. H., Hecky, R. E., Lam, D. C. L., & Schertzer, W. M. (2005). Modeling as a
744 Tool for Nutrient Management in Lake Erie: a Hydrodynamics Study. *Journal of Great Lakes Research*, 31,
745 309-318. doi: 10.1016/S0380-1330(05)70323-3

746 Lick, W., Lick, J., & Kirk Ziegler, C. (1994). The Resuspension and Transport of Fine-Grained Sediments in Lake
747 Erie. *Journal of Great Lakes Research*, 20(4), 599-612. doi: 10.1016/S0380-1330(94)71181-3

748 Lin, S., Boegman, L., & Rao, Y. R. (2021a). Characterizing spatial and temporal distributions of turbulent mixing
749 and dissipation in Lake Erie. *Journal of Great Lakes Research*, 47(1), 168-179.
750 doi:10.1016/j.jglr.2020.11.014

751 Lin, S., Boegman, L., Valipour, R., Bouffard, D., Ackerman, J. D., & Zhao, Y. (2021b). Three-dimensional
752 modeling of sediment resuspension in a large shallow lake. *Journal of Great Lakes Research*, 47(4), 970-
753 984. doi: 10.1016/j.jglr.2021.04.014

754 Liu, W., Bocaniov, S. A., Lamb, K. G., & Smith, R. E. H. (2014). Three dimensional modeling of the effects of
755 changes in meteorological forcing on the thermal structure of Lake Erie. *Journal of Great Lakes Research*,
756 40(4), 827-840. doi: 10.1016/j.jglr.2014.08.002

757 Lohrmann, A. (2001). Monitoring sediment concentration with acoustic backscattering instruments. *Nortek*
758 *Technical Note*, 3, 1-5.

759 Lorke, A. (2007). Boundary mixing in the thermocline of a large lake. *Journal of Geophysical Research: Oceans*,
760 112(C9). doi: 10.1029/2006JC004008

761 Lou, J., Schwab, D. J., Beletsky, D., & Hawley, N. (2000). A model of sediment resuspension and transport
762 dynamics in southern Lake Michigan. *Journal of Geophysical Research: Oceans*, 105(C3), 6591-6610. doi:
763 10.1029/1999JC900325

764 McGinnis, D. F., Sommer, S., Lorke, A., Glud, R. N., & Linke, P. (2014). Quantifying tidally driven benthic oxygen
765 exchange across permeable sediments: An aquatic eddy correlation study. *Journal of Geophysical Research:*
766 *Oceans*, 119(10), 6918-6932. doi: 10.1002/2014JC010303

767 Morales-Marin, L. A., French, J. R., Burningham, H., & Battarbee, R. W. (2018). Three-dimensional hydrodynamic
768 and sediment transport modeling to test the sediment focusing hypothesis in upland lakes. *Limnology and*
769 *Oceanography*, 63(S1), S156-S176. doi: 10.1002/lno.10729

770 Niu, Q., Xia, M., Ludsin, S. A., Chu, P. Y., Mason, D. M., & Rutherford, E. S. (2018). High-turbidity events in
771 Western Lake Erie during ice-free cycles: Contributions of river-loaded vs. resuspended sediments.
772 *Limnology and Oceanography*, 63(6), 2545-2562. doi: 10.1002/lno.10959

773 Paerl, H. W., Hall, N. S., & Calandrino, E. S. (2011). Controlling harmful cyanobacterial blooms in a world
774 experiencing anthropogenic and climatic-induced change. *Science of The Total Environment*, 409(10),
775 1739-1745. doi: 10.1016/j.scitotenv.2011.02.001

776 Pope, S. B. (2000). *Turbulent Flows*. Cambridge, U.K.: Cambridge Univ. Press.

777 Quaresma, L. S., Vitorino, J., Oliveira, A., & da Silva, J. (2007). Evidence of sediment resuspension by nonlinear
778 internal waves on the western Portuguese mid-shelf. *Marine Geology*, 246(2), 123-143. doi:
779 10.1016/j.margeo.2007.04.019

780 Rao, Y. R., Hawley, N., Charlton, M. N., & Schertzer, W. M. (2008). Physical processes and hypoxia in the central
781 basin of Lake Erie. *Limnology and Oceanography*, 53(5), 2007-2020. doi: 10.4319/lo.2008.53.5.2007

782 Salim, S., Pattiaratchi, C., Tinoco, R. O., & Jayaratne, R. (2018). Sediment Resuspension Due to Near-Bed
783 Turbulent Effects: A Deep Sea Case Study on the Northwest Continental Slope of Western Australia.
784 *Journal of Geophysical Research: Oceans*, 123(10), 7102-7119. doi: 10.1029/2018JC013819

785 Sheng, Y. P., & Lick, W. (1979). The transport and resuspension of sediments in a shallow lake. *Journal of*
786 *Geophysical Research: Oceans*, 84(C4), 1809-1826. doi: 10.1029/JC084iC04p01809

787 Shields, A. F. (1936). Application of similarity principles and turbulence research to bed-load movement. Pasadeza,
788 California. California Institute of Technology.

789 Soulsby, R. L., Atkins, R., & Salkield, A. P. (1994). Observations of the turbulent structure of a suspension of sand
790 in a tidal current. *Continental Shelf Research*, 14(4), 429-435. doi: 10.1016/0278-4343(94)90027-2

791 Soulsby, R. L. (1983). Chapter 5 The Bottom Boundary Layer of Shelf Seas. In B. Johns (Ed.), *Elsevier*
792 *Oceanography Series* (Vol. 35, pp. 189-266): Elsevier.

793 Soulsby, R. L., & Whitehouse, R. J. S. (1997). *Threshold of sediment motion in coastal environments*. Paper
794 presented at the Proceedings of the 13th Australasian Coastal and Ocean Engineering Conference and the
795 6th Australasian Port and Harbour Conference.

796 Spigel, R. H., Imberger, J., & Rayner, K. N. (1986). Modeling the diurnal mixed layer. *Limnology and*
797 *Oceanography*, 31(3), 533-556. doi: 10.4319/lo.1986.31.3.0533

798 Stapleton, K. R., & Huntley, D. A. (1995). Seabed stress determinations using the inertial dissipation method and the
799 turbulent kinetic energy method. *Earth Surface Processes and Landforms*, 20(9), 807-815. doi:
800 10.1002/esp.3290200906

801 Valipour, R., Boegman, L., Bouffard, D., & Rao, Y. R. (2017). Sediment resuspension mechanisms and their
802 contributions to high-turbidity events in a large lake. *Limnology and Oceanography*, 62(3), 1045-1065. doi:
803 10.1002/lno.10485

804 Valipour, R., Bouffard, D., & Boegman, L. (2015a). Parameterization of bottom mixed layer and logarithmic layer
805 heights in central Lake Erie. *Journal of Great Lakes Research*, 41(3), 707-718. doi:
806 10.1016/j.jglr.2015.06.010

807 Valipour, R., Bouffard, D., Boegman, L., & Rao, Y. R. (2015). Near-inertial waves in Lake Erie. *Limnology and*
808 *Oceanography*, 60(5), 1522-1535. doi: 10.1002/lno.10114

809 Van Rijn, L. C. (1990). *Principles of Fluid Flow and Surface Waves in Rivers, Estuaries, Seas and Oceans* (Vol. 12).
810 Amsterdam: Aqua Publications.

811 Van Rijn, L. C. (1993). *Principles of Sediment Transport in Rivers, Estuaries and Coastal Seas* (Vol. 1006).
812 Amsterdam: Aqua publications.

813 Voulgaris, G., & Trowbridge, J. H. (1998). Evaluation of the Acoustic Doppler Velocimeter (ADV) for Turbulence
814 Measurements*. *Journal of Atmospheric and Oceanic Technology*, 15(1), 272-289. doi:10.1175/1520-
815 0426(1998)015<0272:EOTADV>2.0.CO;2

816 Warner, J. C., Sherwood, C. R., Signell, R. P., Harris, C. K., & Arango, H. G. (2008). Development of a three-
817 dimensional, regional, coupled wave, current, and sediment-transport model. *Computers & Geosciences*,
818 34(10), 1284-1306. doi: 10.1016/j.cageo.2008.02.012

819 Yang, Y., Wang, Y. P., Gao, S., Wang, X. H., Shi, B. W., Zhou, L., Wang, D. D., Dai, C., & Li, G. C. (2016).
820 Sediment resuspension in tidally dominated coastal environments: new insights into the threshold for initial
821 movement. *Ocean Dynamics*, 66(3), 401-417. doi:10.1007/s10236-016-0930-6

822 Yuan, Y., Wei, H., Zhao, L., & Cao, Y. (2009). Implications of intermittent turbulent bursts for sediment
823 resuspension in a coastal bottom boundary layer: A field study in the western Yellow Sea, China. *Marine*
824 *Geology*, 263(1), 87-96. doi: 10.1016/j.margeo.2009.03.023
825 Zurberti, A. P., Ivey, G. N., & Jones, N. L. (2018). *Observations of near-bed stress beneath nonlinear internal wave*
826 *trains in the ocean*. Paper presented at the 21st Australasian Fluid Mechanics Conference, Adelaide,
827 Australia.

830 **Fig. 1.** (a) Map of Lake Erie showing the location of field observation (Sta. 341) and National Data Buoy Center
831 (NDBC) wave buoy (45005). Negative numbers show the depth contours in meters. Red triangles are the sources of
832 meteorological data used to drive the AEM3D and ELCOM models. (b) The tripod equipped with ADCPs, an ADV
833 and RBR TR-1060s before deployment on the lakebed at Sta. 341 in 2008. (c) West-to-east curtain showing vertical
834 grid (z-level) spacing in the models.

835 **Fig. 2.** Time-series at Sta. 341 for 2008 (a) wind speed (blue line; left y-axis) and direction (red dashed line; right y-
836 axis) at 10 m above water surface, (b) turbidity at 1.5 mab from XR-620 (black stars) and its 7-day moving mean
837 (grey line) and 7-day standard deviation (grey shading), (c) ADV-amp at 1 mab (blue dots) and its 7-day moving
838 mean (blue line) and 7-day standard deviation (blue shading), (d) τ_L (purple dash-dot line, Eq. 10), τ_{TKE} (green
839 dash-dot line, Eq. 5) and critical value for resuspension ($\tau_{cr}=0.045$ Pa; black dashed line), (e) τ_w (blue line, Eq. 6),
840 τ_c (red line, Eq. 9) and τ_{cr} , (f-h) Modeled $\tau_{c,m}$ and $\tau_{w,m}$ based on varying C_D and algorithms.

841 **Fig. 3.** Time-series at Sta. 341 for first deployment in 2009 (a) wind speed (blue line; left y-axis) and direction (red
842 dashed line; right y-axis) at 10 m above water surface, (b) turbidity at 1.5 mab from XR-620 (black stars) and its 7-
843 day moving mean (grey line) and standard deviation (grey shading) (left y-axis). Green stars are *Chl-a* concentration
844 at 5 mab from XR-420 (right y-axis), (c) ADV-amp at 1 mab (blue dots) and its 7-day moving mean (blue line) and
845 standard deviation (blue shading). Color bar shows the ADCP echo level, (d) τ_L (purple dash-dot line, Eq. 10), τ_{TKE}
846 (green dash-dot line, Eq. 5) and τ_{cr} (black dashed line), (e) τ_w (blue line, Eq. 6), τ_c (red line, Eq. 9) and τ_{cr} , (f-g)
847 Modeled $\tau_{c,m}$ and $\tau_{w,m}$ based on the algorithms in AEM3D with varying C_D (h) Modeled $\tau_{c,m}$ and $\tau_{w,m}$ based on
848 the algorithms in ELCD.

849 **Fig. 4.** Time-series at Sta. 341 for second deployment in 2009 (a) wind speed (blue line; left y-axis) and direction
850 (red dashed line; right y-axis) at 10 m above water surface, (b) turbidity at 1.5 mab from XR-620 (black stars) and
851 its 7-day moving mean (grey line) and standard deviation (grey shading), and green shading indicates the high
852 turbidity from algae (Paerl et al., 2011), (c) ADV-amp at 1 mab (blue dots) and its 7-day moving mean (blue line)
853 and standard deviation (blue shading), (d) τ_L (purple dash-dot line, Eq. 10), τ_{TKE} (green dash-dot line, Eq. 5) and
854 τ_{cr} (black dashed line), (e) τ_w (blue line, Eq. 6), τ_c (red line, Eq. 9) and τ_{cr} , (f-g) Modeled $\tau_{c,m}$ and $\tau_{w,m}$ based on
855 the algorithms in AEM3D with varying C_D (h) Modeled $\tau_{c,m}$ and $\tau_{w,m}$ based on the algorithms in ELCD.

856 **Fig. 5** Details of resuspension events R21-23 in Fig. 4. Time-series at Sta. 341 of (a-c) wind speed (blue lines; left
857 y-axis) and direction (red dashed lines; right y-axis) at 10 m above water surface, (b-f) turbidity at 1.5 mab from
858 XR-620 (black stars) and its 7-day moving mean (grey line) and standard deviation (grey shading), (g-i) ADV-amp
859 at 1 mab (right y-axis), and its 7-day moving mean (blue line) and standard deviation (blue shading), (j-l) show τ_{TKE}
860 (purple dash-dot line, Eq. 5) and τ_L (green dash-dot line, Eq. 10) based on turbulent velocity from ADV, and *in situ*
861 critical value for resuspension $\tau_{cr} = 0.045$ Pa, (m-o) τ_w (blue line, Eq. 6) based NDBC station 45005, τ_c (red line,

862 Eq. 9) based on mean current velocity from ADV, and τ_{cr} (black dashed line), (p-r) AEM3D output $\tau_{w,m}$ (blue
863 dotted line) and $\tau_{c,m}$ (red dotted line) used $C_D = 0.0024$, (s-u) AEM3D output $\tau_{w,m}$ (blue dashed line) and $\tau_{c,m}$ (red
864 dashed line) used $C_D = 0.0045$; and (v-x) are ELCD output $\tau_{w,m}$ (blue dashed line) and $\tau_{c,m}$ (red dashed line).

865 **Fig. 6** Details of resuspension events R14, 15, 17 in Fig. 3. Time-series at Sta. 341 of (a-c) wind speed (blue lines;
866 left y-axis) and direction (red dashed lines; right y-axis) at 10 m above water surface, (b-f) turbidity at 1.5 mab from
867 XR-620 (black stars) and its 7-day moving mean (grey line) and standard deviation (grey shading), green shading
868 indicates the high turbidity from algae (Paerl et al., 2011), (g-i) ADV-amp at 1 mab (right y-axis), and its 7-day
869 moving mean (blue line) and standard deviation (blue shading), (j-l) show τ_{TKE} (purple dash-dot line, Eq. 5) and τ_L
870 (green dash-dot line, Eq. 10) based on turbulent velocity from ADV, and *in situ* critical value for resuspension $\tau_{cr} =$
871 0.045 Pa, (m-o) τ_w (blue line, Eq. 6) based NDBC station 45005, τ_c (red line, Eq. 9) based on mean current velocity
872 from ADV, and τ_{cr} (black dashed line), (p-r) AEM3D output $\tau_{w,m}$ (blue dotted line) and $\tau_{c,m}$ (red dotted line) used
873 $C_D = 0.0024$; (s-u) AEM3D output $\tau_{w,m}$ (blue dashed line) and $\tau_{c,m}$ (red dashed line) used $C_D = 0.0045$, and (v-x)
874 are ELCD output $\tau_{w,m}$ (blue dashed line) and $\tau_{c,m}$ (red dashed line).

875 **Fig. 7** Details of resuspension events R7, 10, 12 in Fig. 2, 3. Time-series at Sta. 341 of (a-c) wind speed (blue lines;
876 left y-axis) and direction (red dashed lines; right y-axis) at 10 m above water surface, (b-f) turbidity at 1.5 mab from
877 XR-620 (black stars) and its 7-day moving mean (grey line) and standard deviation (grey shading), and Chl-a
878 concentration at 5 mab from XR-420 (right y-axis), (g-i) ADV-amp at 1 mab (right y-axis), its 7-day moving mean
879 (blue line) and standard deviation (blue shading), and colorbar shows the ADCP echo level; (j-l) show τ_{TKE} (purple
880 dash-dot line, Eq. 5) and τ_L (green dash-dot line, Eq. 10) based on turbulent velocity from ADV, and *in situ* critical
881 value for resuspension ($\tau_{cr} = 0.045$ Pa; black dashed line); (m-o) τ_w (blue line, Eq. 6) based NDBC station 45005,
882 τ_c (red line, Eq. 9) based on mean current velocity from ADV, and τ_{cr} (black dashed line); (p-r) AEM3D output
883 $\tau_{w,m}$ (blue dotted line) and $\tau_{c,m}$ (red dotted line) used $C_D = 0.0024$; (s-u) AEM3D output $\tau_{w,m}$ (blue dashed line)
884 and $\tau_{c,m}$ (red dashed line) used $C_D = 0.0045$; and (v-x) are ELCD output $\tau_{w,m}$ (blue dashed line) and $\tau_{c,m}$ (red
885 dashed line).

886 **Fig. 8** Details of resuspension events R6 in Fig. 2. Time-series at Sta. 341 of 2008 (a) wind speed (left y-axis) and
887 direction (right y-axis) at 10 m above water surface, (b) temperature contours from TR-1060 temperature loggers,
888 red arrows show vertical locations of temperature loggers, (c) turbidity at 1.5 mab from XR-620 (left y-axis), and
889 ADV-amp at 1 mab (right y-axis); (d) and (e) show τ_L (green dash-dot line, Eq. 10), τ_{TKE} (purple dash-dot line, Eq.
890 5), τ_w (blue line, Eq. 6), τ_c (red line, Eq. 9) based on observed data and τ_{cr} (black dashed line); (f) and (g) are ELCD
891 output of temperature and TSS concentration at Sta. 341, respectively.

892 **Fig. 9** Time-series at Sta. 341 of τ_L (Eq. 11) based on ε_m (Eq. 16, orange line) and ε_{ID} (green dash-dot line).

893 Comparisons of observed and modelled turbulent dissipation are shown in Fig. S6.

894 **Fig. 10** Mean value of AEM3D modeled $\tau_{w,m}$, $\tau_{c,m}$, and τ_b (a-c) over spring and summer (days 203 – 245 of 2008
895 and days 119- 250 of 2009), and (d-f) over fall (days 245- 303 of 2008 and days 250 – 300 of 2009).

896 **Table 1** Assessment of bottom stress parameterization in ELCD (denoted by m1) and AEM3D (denoted by m2, 3)
897 models.

898 **Table 2** Parameterizations for τ_c in different sediment models. The equations in column 2 were solved using
899 parameters characteristic to Lake Erie (column 4).

Figure 1.

Figure 2.

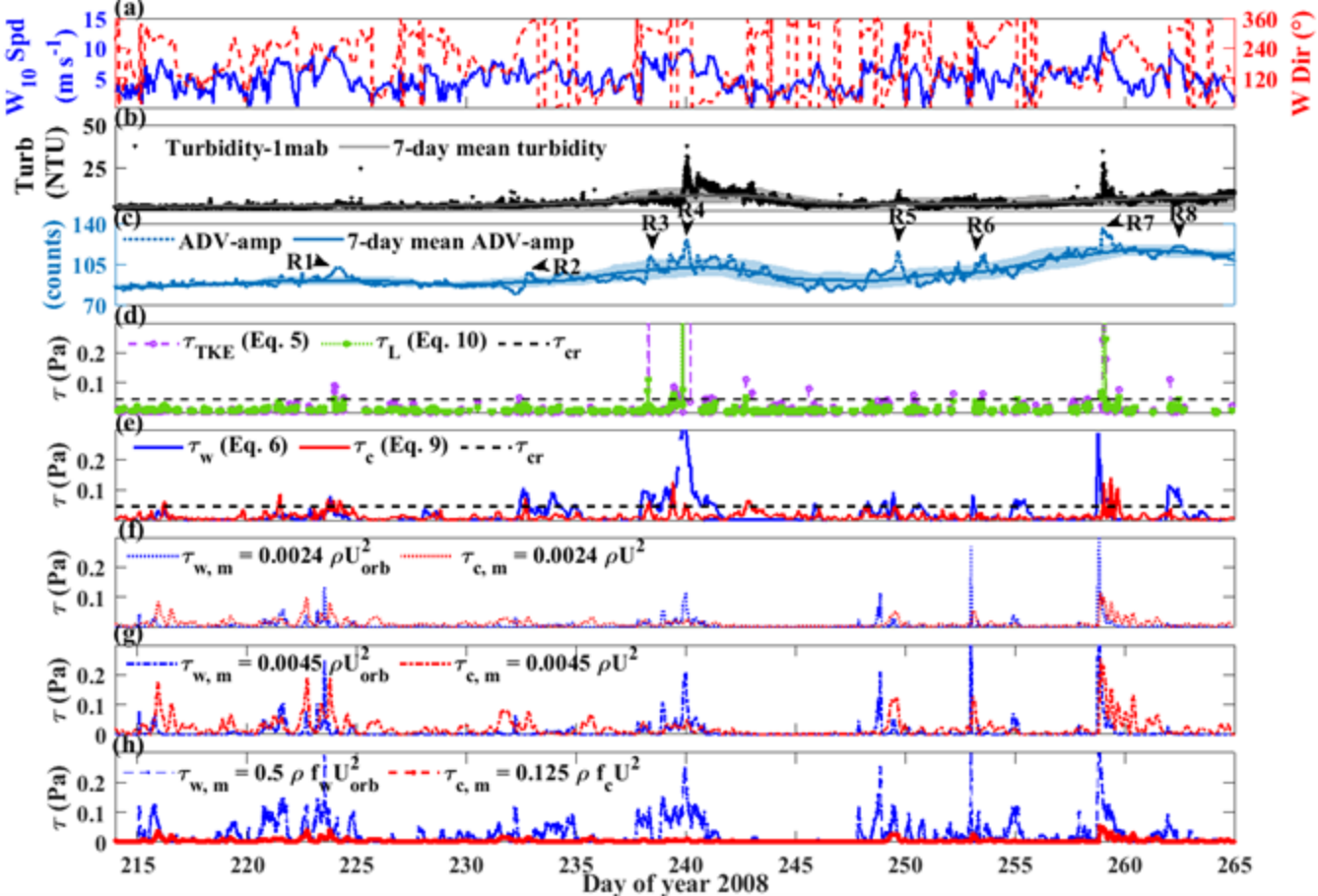


Figure 3.

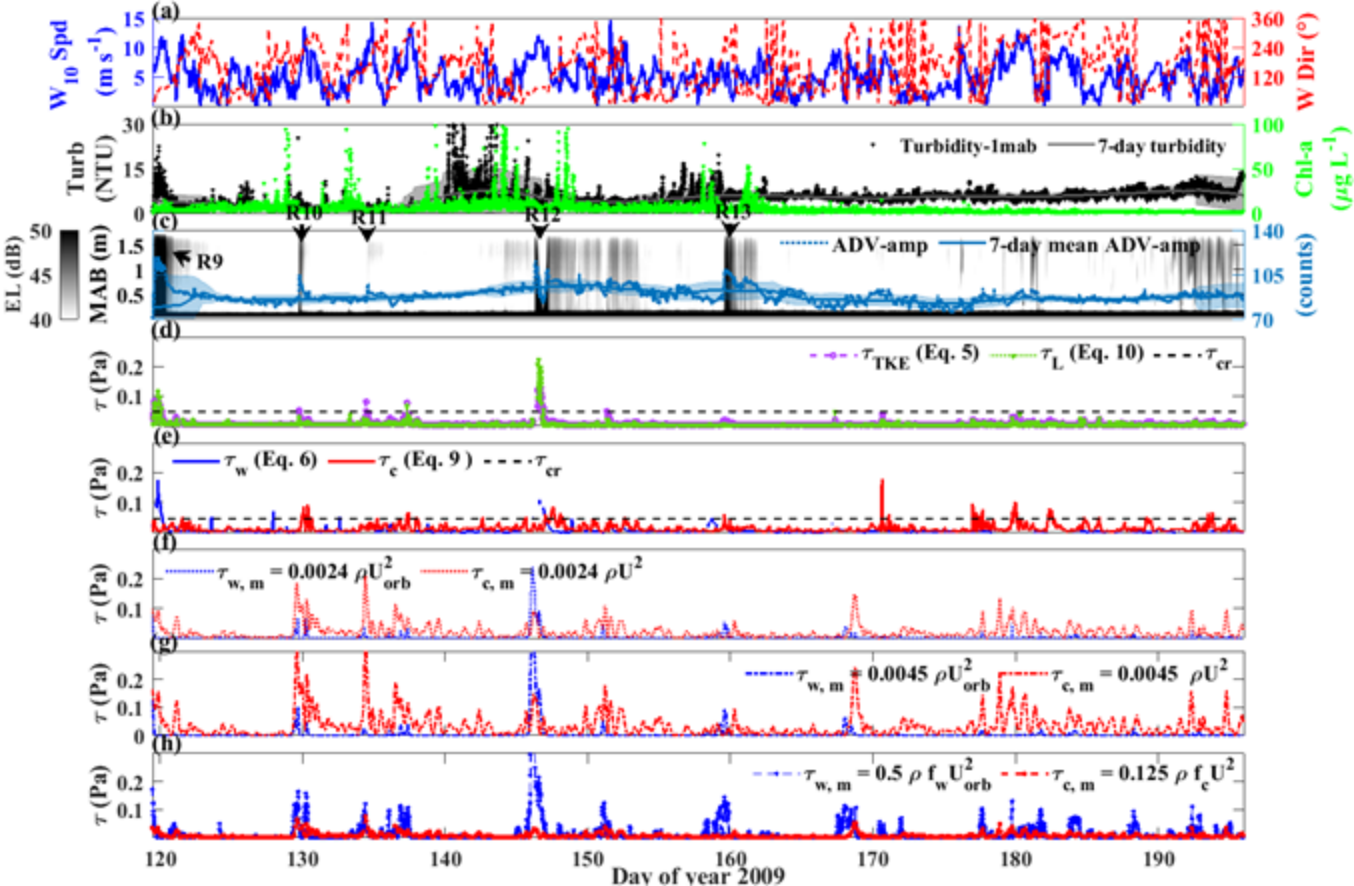


Figure 4.

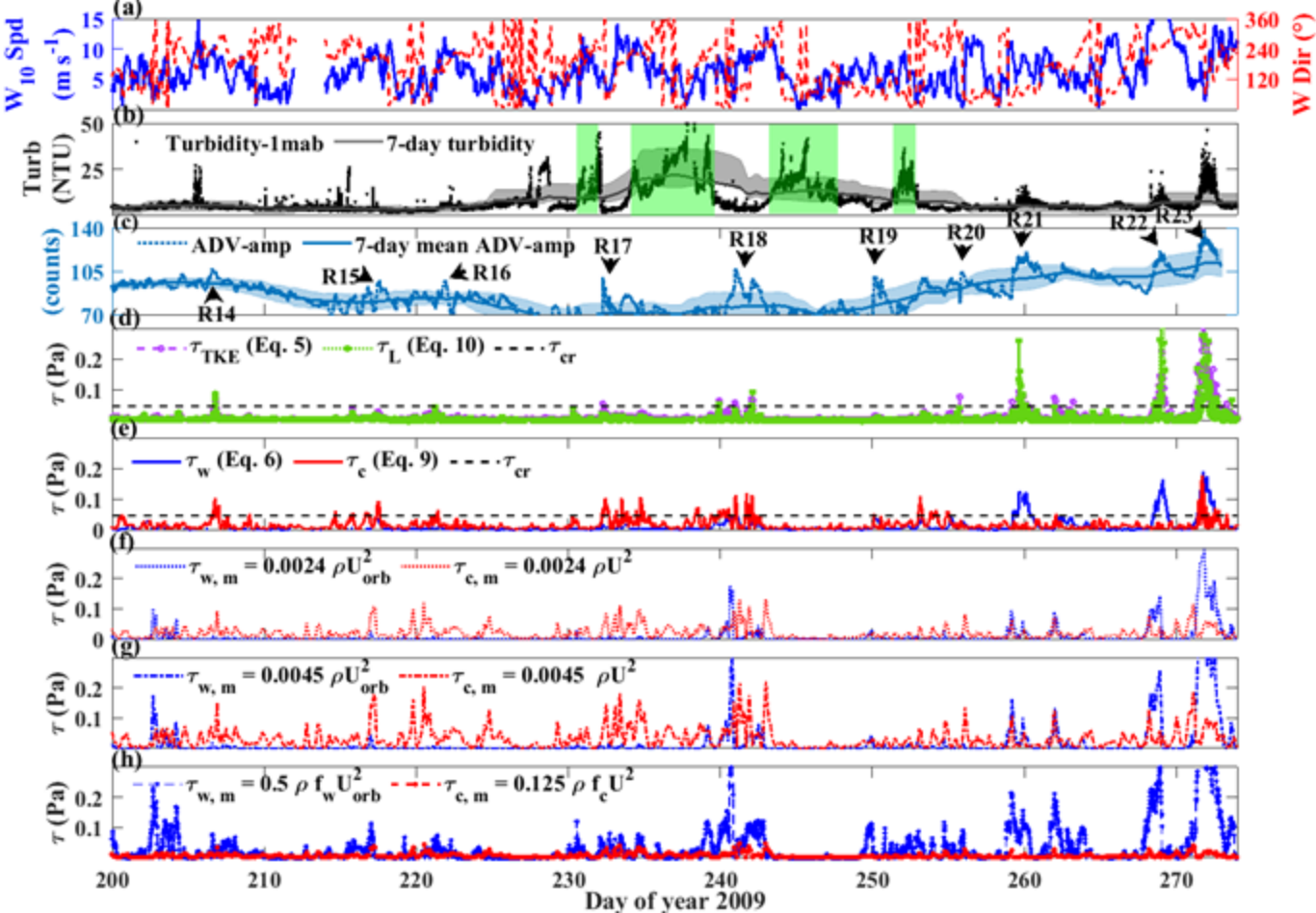


Figure 5.

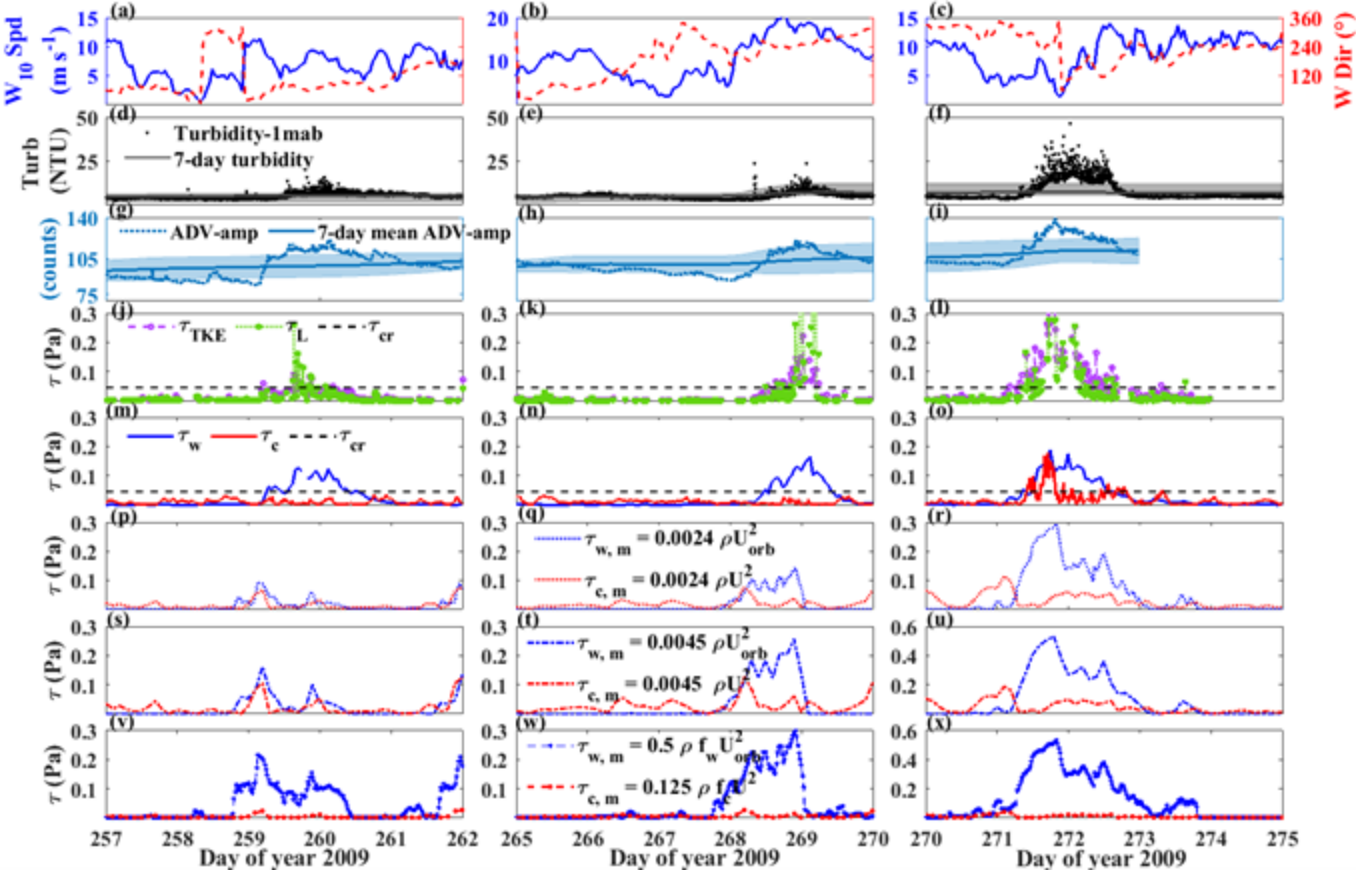


Figure 6.

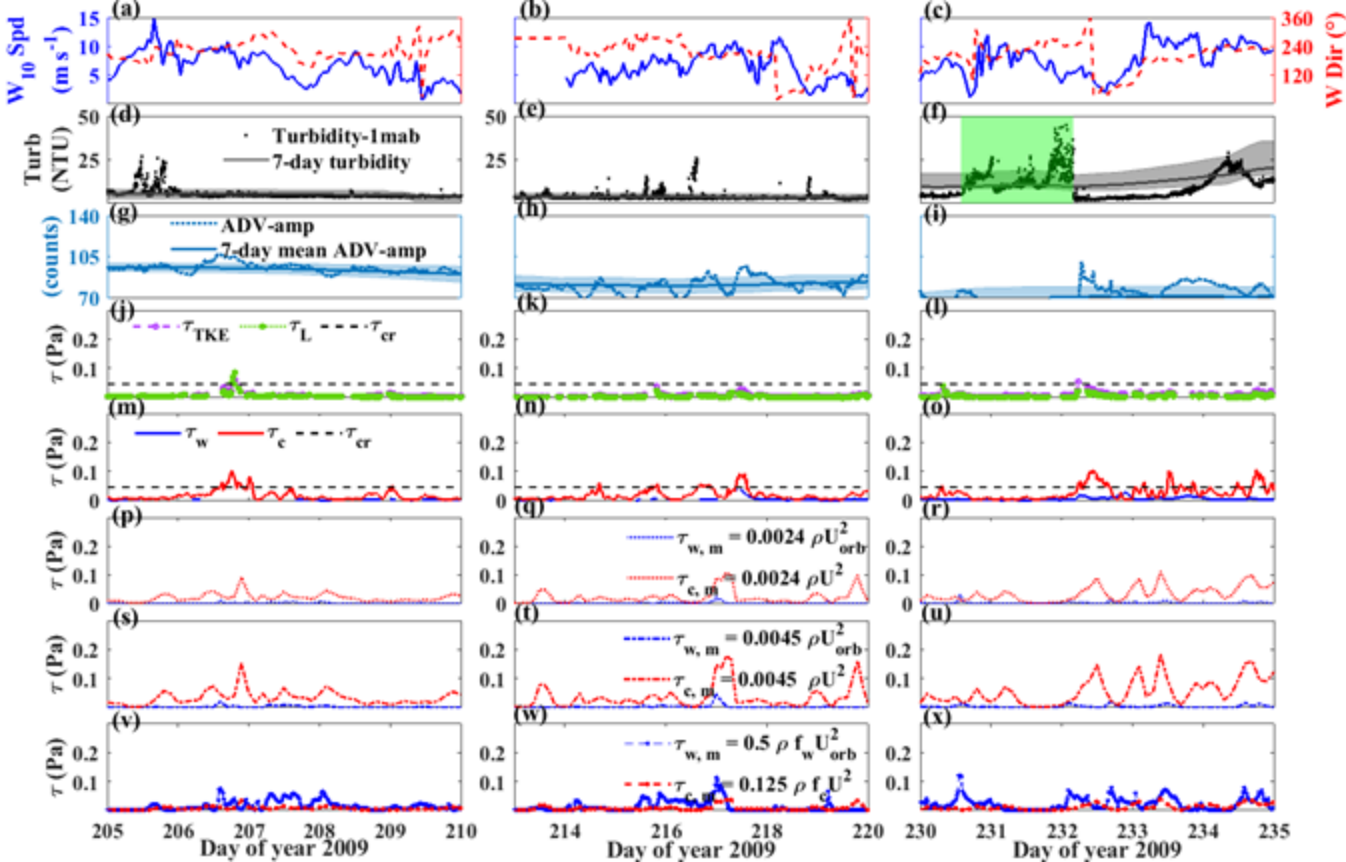


Figure 7.

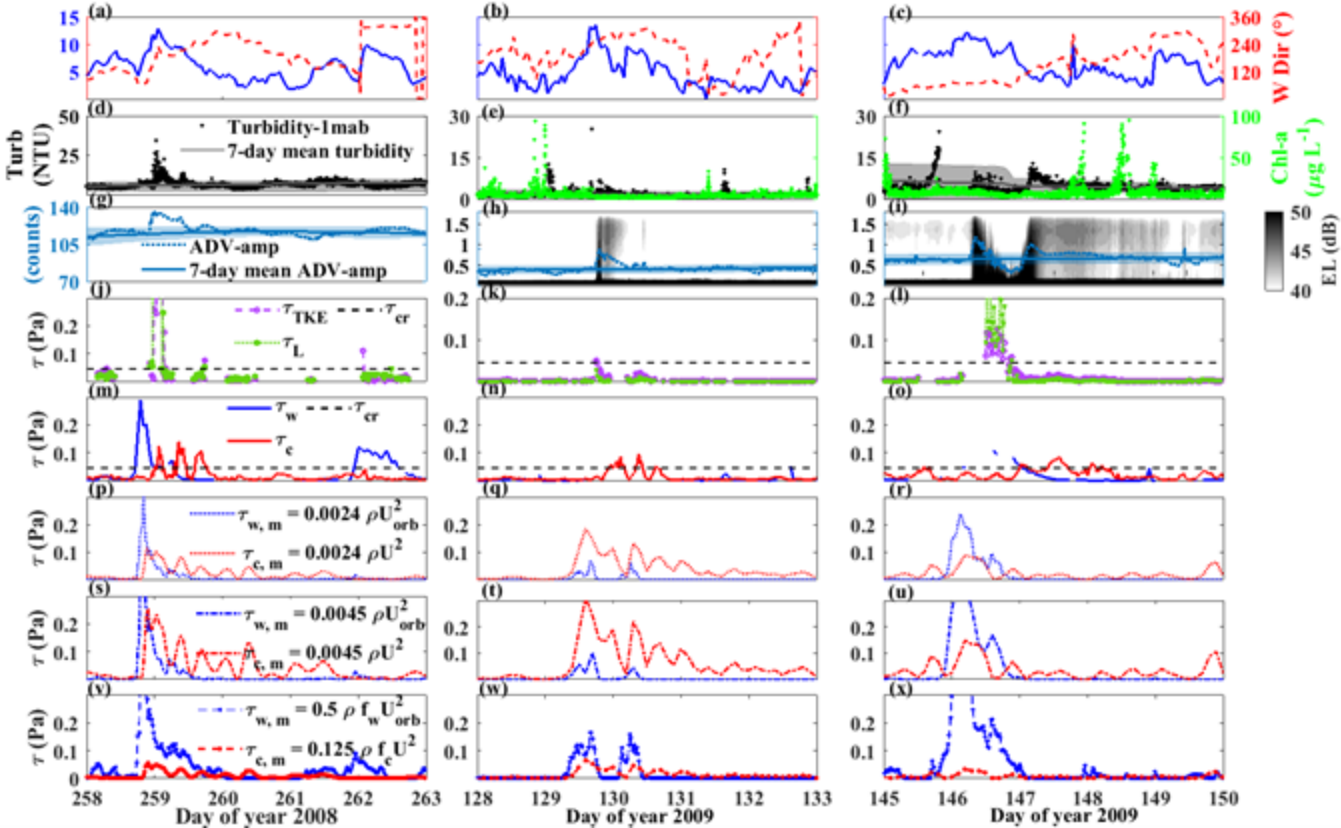


Figure 8.

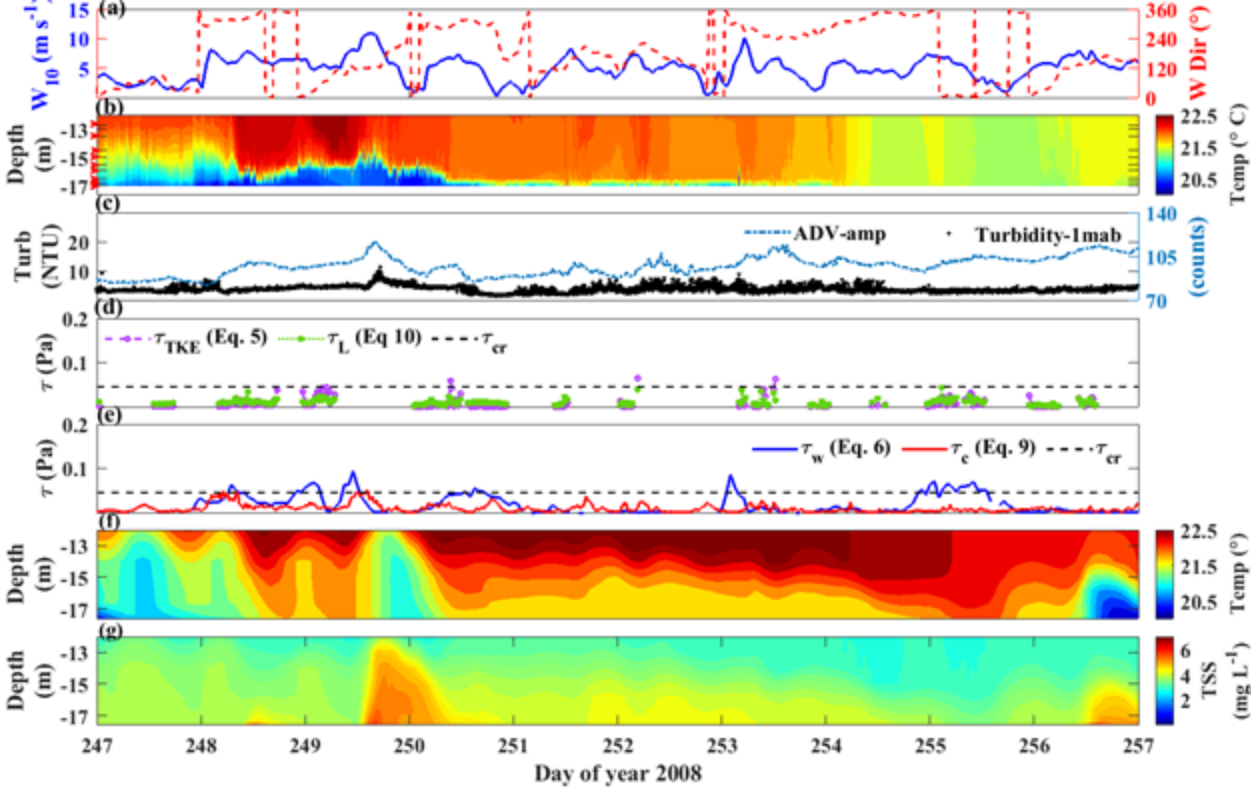


Figure 9.

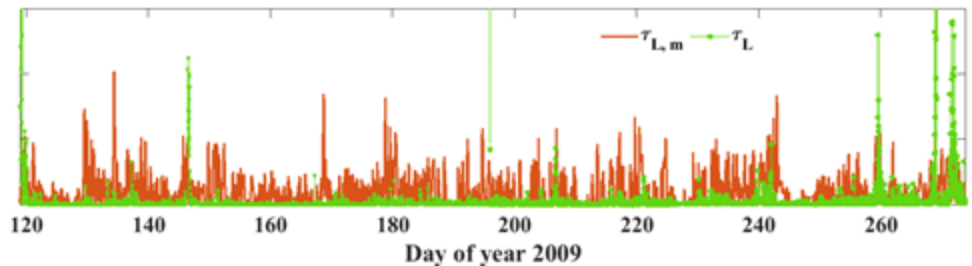
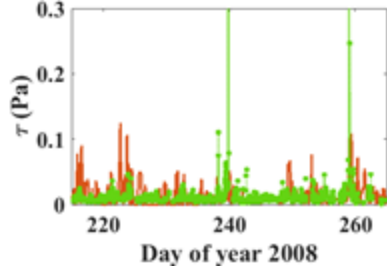


Figure 10.

